



Unprecedented roles of submillimetric interelectrode distances and electrogenerated gas bubbles on mineral cathodic electroprecipitation: modeling and interface studies

Faidzul Hakim Adnan, Steve Pontvianne, Marie-Noëlle Pons, Emmanuel Mousset, Faidzul Hakim Adnan

► To cite this version:

Faidzul Hakim Adnan, Steve Pontvianne, Marie-Noëlle Pons, Emmanuel Mousset, Faidzul Hakim Adnan. Unprecedented roles of submillimetric interelectrode distances and electrogenerated gas bubbles on mineral cathodic electroprecipitation: modeling and interface studies. Chemical Engineering Journal, 2022, 431 (Part 4), pp.133413. 10.1016/j.cej.2021.133413 . hal-03576623

HAL Id: hal-03576623

<https://hal.science/hal-03576623>

Submitted on 16 Feb 2022

HAL is a multi-disciplinary open access archive for the deposit and dissemination of scientific research documents, whether they are published or not. The documents may come from teaching and research institutions in France or abroad, or from public or private research centers.

L'archive ouverte pluridisciplinaire **HAL**, est destinée au dépôt et à la diffusion de documents scientifiques de niveau recherche, publiés ou non, émanant des établissements d'enseignement et de recherche français ou étrangers, des laboratoires publics ou privés.

Unprecedented roles of submillimetric interelectrode distances and electrogenerated gas bubbles on mineral cathodic electro- precipitation: modeling and interface studies

Faidzul Hakim Adnan¹, Steve Pontvianne¹, Marie-Noëlle Pons^{1,2}, Emmanuel Mousset^{1,*}

¹ *Université de Lorraine, CNRS, LRGP, F-54000 Nancy, France*

² *LTSE-LRGP, CNRS, Université de Lorraine, F-54000 Nancy, France*

VERSION ACCEPTEE DANS

CHEMICAL ENGINEERING JOURNAL

2022

*Contact of corresponding author: emmanuel.mousset@cnrs.fr

ABSTRACT

For the first time, the roles of submillimetric interelectrode distances (d_{elec}) and electrogenerated gas on cathodic mineral electro-precipitation have been investigated, particularly under advanced electro-oxidation condition with boron-doped diamond (BDD) anode. The main objective was to understand how to limit or favor the magnesium hydroxide ($\text{Mg}(\text{OH})_2$) and calcium carbonate (CaCO_3) deposits that progressively passivate the cathode surface during the electrolysis of effluent initially containing calcium (Ca^{2+}), magnesium (Mg^{2+}) and bicarbonate/carbonate ($\text{HCO}_3^-/\text{CO}_3^{2-}$). As predicted by a new model taking into account the concomitant H_2 evolution reaction (HER), more mineral scaling ($\text{Mg}(\text{OH})_2$ and CaCO_3) was observed in decreasing order of d_{elec} from 3 mm to 100 μm at 4 mA cm^{-2} . Contrastingly, no deposit was present at the lowest d_{elec} (50 μm), which was due to non-faradaic condition. The applied cathode potential (E_C) decreased with increase of d_{elec} , which intensified the H_2 gas bubbles production and minimized the electro-precipitation. Supplementary experiments with identical E_C highlighted the additional involvement of O_2 evolution at the anode towards the cathodic mineral scaling, whose role was intensified at submillimetric distances. Finally, novel predictive correlations have been proposed from impedance spectroscopy studies at cathode/electrolyte interface in order to link the charge transfer resistance (R_{CT}) and the double-layer capacitance (C_{DL}) with d_{elec} .

Keywords: anodic oxidation, electrochemical engineering, impedance, microfluidic, reactor design, scaling

1. Introduction

It is now well-established that a gradient of hydroxyl ions (OH^-) concentration occurs during the electrolysis of aqueous media between cathode vicinity and bulk solution due to reduction reactions of dissolved oxygen (O_2) (Eq. (1)) and/or water (H_2O) (Eq. (2)) [1-3]:



In the presence of calcium (Ca^{2+}) and magnesium (Mg^{2+}) ions, precipitates of hydroxide might occur (Eqs. (3)-(4)) [4]. The local pH increment also shifts thermodynamic ratio of bicarbonates/carbonates (Eq. (5)) in favors of calcareous deposit formation following Eq. (6) [5, 6].



When an electrochemical cell is to be used in electrochemical advanced oxidation processes (EAOP) to treat wastewater [7-11], these deposits present a major drawback. Calcareous deposits on electrode cause a non-conductive physical barrier on its surface. This phenomenon is called cathode passivation and reduces significantly the current density distribution, thus compromising the electrochemical process in long-term run.

The application of microfluidic reactors within the framework of EAOPs has risen the bar in the perspective of wastewater treatment capability [12-15]. Coupled to the development of diamond-based anode or other high overpotential for oxygen evolution reaction (OER), higher degree of electrochemical oxidation of organic contaminants has been reached [16-19]. The micrometric

interelectrode distances (d_{elec}) not only allow mineralization of organic pollutants without the addition of supporting electrolyte but they also vastly accommodate the phenomenon of limitation by mass transfer and ohmic resistance [20]. This is particularly adequate with solutions having low ionic conductivity, which is typical of the effluent at the outlet of municipal WWTPs [21-23].

Numerous studies have already been reported about the formation of mineral scaling in electrochemical cells while treating different water sources originated from different domains of application: artificial water for cooling system in cooling towers and oil refineries [24, 25], artificial [26, 27] and natural underground water [28, 29], mineral potable water [30, 31], artificial [4, 6, 32, 33] and real seawater [34, 35]. Most of the works were carried out using rotating disk electrodes (RDE) possessing effective surface area of 0.2 cm² [4, 6, 26-30, 34], 0.5 cm² [24, 25, 36], 1 cm² [33, 37, 38] and 1.5 cm² [32]. Recently, more scalable electrochemical cell geometries were suggested to study the occurrence of mineral electro-precipitation. Artificial brine solution (25 mL) was used to precipitate Ca and Mg deposits on cathode with 0.75 cm² effective surface area in a parallel-plate electrochemical cell working in discontinuous mode [39, 40]. The cathode and anode were separated by a 5 mm gap. In another series of work, horizontal parallel-plate cell with higher geometric surface area (i.e. 36 cm²) was equipped to electrochemically precipitate calcium, magnesium and phosphorus [41-44]. 0.8 to 1 L wastewater effluent was electrolyzed in recirculation mode and the distance separating anode and cathode in these works was 30 mm. Elsewhere, Sanjuán et al. in their work conducted a water hardness treatment of simulated electrodialysis concentrate [45]. The studies were done in a flow plant equipped with commercial undivided cell possessing electrodes with 100 cm² surface area. Our recent work [46] was the first to illustrate the occurrence of mineral scaling inside a parallel-plate (surface area: 50 cm²) microfluidic reactor at a given d_{elec} (500 μm) where the influence of electrolytic composition and current density were scrutinized. To the best of authors' knowledge, no report has yet been published to discuss the variation of mineral deposition with d_{elec} lower than 5 mm, especially at submillimetric distances that imply a different mass transfer behavior. Moreover, it is known that

electro-precipitation often takes place with concomitant hydrogen evolution reaction (HER) [37, 38, 47-49]. It results in calcareous deposit with porous morphology and is also the reason for partial deposit detachment from cathode surface [36, 38, 48, 50]. However, the role of gas evolution on electro-precipitation in submillimetric distances has never been explored. Furthermore, mass transfer intensification would promote the involvement of O₂ gas generated from OER at anode under micrometric configuration.

For the first time, the influence of a wide range of d_{elec} (50-3000 μm) with regard to the occurrence of cathodic mineral deposition is therefore investigated in details. The involvement of HER while varying d_{elec} and its effect towards the quantity of mineral scaling is further scrutinized. A new kinetic model has been proposed to predict the electro-precipitation at the different d_{elec} , by incorporating the gas evolution. To reinforce the mechanistic understanding at the cathode/electrolyte interface over the wide range of investigated d_{elec} , electrochemical impedance spectroscopy (EIS) analysis have been performed.

2. Material and methods

2.1. Chemicals

Calcium sulfate dihydrate (>90%), magnesium sulfate heptahydrate (>98%), sodium hydrogenocarbonate (>99.5%) and sodium sulfate (>97%) were obtained from VWR International (Fontenay-sous-Bois, France). Sulfuric acid (95-97%) was provided by Sigma Aldrich (Saint-Quentin-Fallavier, France). These chemical reagents were used as purchased without further treatment.

2.2. Preparation of electrolyte

Artificial electrolyte contained fixed concentration of Ca²⁺ (150 mg L⁻¹), Mg²⁺ (5 mg L⁻¹) and 60 mg-C L⁻¹ carbonates, which were obtained by dissolving CaSO₄.2H₂O, MgSO₄.7H₂O and NaHCO₃

in ultrapure water (18.2 M Ω cm) provided by PureLab ELGA Classic water purification system (Veolia Water, Antony, France). Adequate amounts of salts were used to achieve the desired concentrations of Ca²⁺, Mg²⁺ and HCO₃⁻/CO₃²⁻ without further addition of supporting electrolyte. The initial value of pH was adjusted to 7.6 by adding sulfuric acid when necessary. SO₄²⁻ concentration as counter ion was measured at 4.16 mmol L⁻¹. This value of SO₄²⁻ concentration has negligible influence on the electro-migration of reacting elements towards electrodes as previously shown [46]. The mixture of salts including pH adjustment yielded an ionic conductivity of around 1000 μ S cm⁻¹ and ionic strength of 0.02 mol L⁻¹. These properties correspond to the average characteristic of effluent at the outlet of municipal WWTPs.

2.3. Electrochemical system

Experimental pilot and electrochemical cell were described in detail elsewhere [46, 51]. 0.5 L of artificial electrolyte was used and it was stored in a double-jacket stainless steel reservoir equipped with a thermostatic bath (Bioblock Scientific, PolyScience, Niles, IL, USA) to maintain a working temperature of 25°C. A digital peristaltic pump (Masterflex, Cole-Parmer, Vernon Hills, IL, USA) was used to pump the electrolyte in recirculation mode. The electrochemical cell was a parallel-plate reactor. Double-sided boron-doped diamond (BDD) coated on Niobium (Nb) substrate (DiaCCon, Fürth, Germany) with 50 cm² per side effective surface area was used as anode. Stainless steel (SS) (Gantois Industries, Saint-Dié-des-Vosges, France) also with 50 cm² effective surface area was used as cathode. Prior to utilization, SS was preconditioned chemically by soaking in sulfuric acid solution at 0.25 M overnight to get rid of possible remaining mineral deposition. As to avoid contact between anode and cathode, inert non-conducting spacer made of polytetrafluoroethylene (PTFE) (Bohlender, Grünsfeld, Germany) was placed in-between the electrodes. Various thicknesses of the spacer were used: 50, 100, 250 and 500 μ m for micrometric distances as well as 1000 and 3000 μ m for millimetric distances. Unless mentioned otherwise, electrolysis was carried out in galvanostatic mode under the polarization of 4 mA cm⁻² (200 mA)

using current generator HMP4040 (Rohde & Schwarz, Meudon-la-Forêt, France). It was selected since it has been defined as optimal current density to degrade a pharmaceutical pollutant in previous work [21]. All experiments were done at least in duplicate.

Throughout the series of experiments, the applied current density was always higher than all initial limiting current density $j_{lim,0}$ values (Table S1), whatever the configurations used. The $j_{lim,0}$ value for each electrochemical cell setup was evaluated using Eq. (S1) [51]. Therefore, across all configurations from millimetric to microfluidic investigated in this work, the electrochemical processes were considered to be controlled by diffusional mass-transfer. It has also been demonstrated in previous work, that electro-migration has no influence in the range of experimental conditions applied [46]. It is also primordial to mention that while varying d_{elec} , the liquid flow rate was also adjusted to have identical electrolyte residence time across different volumes of electrochemical reactors for relevant comparison. This consideration was also done by Khongthon et al. [52]. The flow rate of 10, 20, 50, 100, 200 and 600 mL min⁻¹ were used for 50, 100, 250, 500, 1000 and 3000 μ m d_{elec} respectively. A residence time of 0.025 min was maintained across all configurations. Since the electrolyte flow rate was adapted accordingly to the volume of reactor, cross-sectional electrolyte velocity was also kept constant, i.e., in this work 4 m min⁻¹, from one configuration to another. Knowing the fact that the hydrodynamic diameter (d_H) (Eq. (S2)) was modified from one d_{elec} to another, Reynolds number (Re) (Eq. (S3)) also increased with the d_{elec} as summarized in Table S1 and Text S1. Re values could be calculated by considering the physicochemical properties of electrolyte presented in Table S2. Re values ranged from 7 (50 μ m) to 377 (3000 μ m) (Table S1), meaning that the hydrodynamic flow of electrolyte was maintained under laminar regime in all investigated cases [51, 53-55]. This could ensure reliable comparisons of the results obtained under different d_{elec} setups.

2.4. Analytical methods

Concentration of Ca and Mg were monitored using inductively coupled plasma optical emission spectroscopy (ICP-OES) Thermo iCAP 6000 (Thermo Fisher, Illkirch-Graffenstaden, France). The samples were filtered using Phenex 0.45 μm filter (Phenomenex, Le Pecq, France) prior to analysis. Total inorganic carbon (TIC) was measured using a TOC-meter V_{CSH} TC/TN (Shimadzu, Marne-La-Vallée, France). Linear scan voltammetry (LSV), chronoamperometry and chronopotentiometry were applied using a potentiostat (Ametek, Massy, France) connected to the electrochemical cell. The electrode potentials were reported as function of saturated silver chloride reference electrode (V/Ag-AgCl). LSV was carried out sweeping the range of cathodic potentials from 0 to -1.6 V/Ag-AgCl using a scan rate of 10 mV s⁻¹. Owing to the integration of frequency response analyzer (FRA) to the potentiostat, EIS can be carried out. EIS was conducted in galvanostatic mode covering the frequency ranges between 100 kHz to 100 mHz. The perturbation amplitude (ΔI_{AC}) varied between 5 and 10 mA root mean square (RMS) according to EIS spectra with 10 points per decade (ppd). The EIS analysis was programmed at regular interval during galvanostatic electrolysis at applied direct current of 200 mA (i.e. 4 mA cm⁻²). The EIS parameters were extracted by means of equivalent electrical circuit (EEC) model using ZSimpwin® commercial software.

2.5. Recovery process of Ca and Mg elements

The recovery procedure was carried out following a method described in detail elsewhere [46]. The objective was to re-dissolve the mineral deposits back into ionic form by lowering the pH. The washing was done on cathode, anode and pilot tubing to ensure a thorough recovery process.

3. Modeling

3.1. Kinetics of Mg(OH)₂ and CaCO₃ electro-precipitation

A kinetic model has been proposed to predict the electro-precipitation by considering the influence of d_{elec} . The methodology given for a single d_{elec} (500 μm) in our previous work has been followed and adapted to take into account the electrodes gap [46]. Local alkalization on cathode surface

occurred due to faradaic reactions of reduction of dissolved O₂ (**Eq. (1)**) and H₂O (**Eq. (2)**), while the OH⁻ production can be estimated by Faraday's law (**Eq. (7)**):

$$r_{OH^-} = + \frac{d[OH^-]}{dt} = \frac{\nu_{O_2} j_{app}}{n_{O_2} F} CE_{O_2} + \left(\nu_{H_2O} \frac{CE_{H_2O}}{n_{H_2O}} - \nu_{H_2} \frac{CE_{H_2}}{n_{H_2}} \right) \frac{j_{app}}{F} \quad (7)$$

where r_{OH^-} is the heterogeneous production rate of OH⁻ (mol m⁻² min⁻¹), n_{O_2} (=4) and n_{H_2O} (=2) are the numbers of electrons participating in **Eq. (1)** and **Eq. (2)** respectively whilst ν_{O_2} (=4) and ν_{H_2O} (=2) are the stoichiometric coefficient of OH⁻ production from **Eq. (1)** and **Eq. (2)** respectively. n_{H_2} (=2) and ν_{H_2} (=1) are respectively the number of electrons reacted and stoichiometry to produce H₂ with respect to the stoichiometry of OH⁻ production from H₂O reduction in **Eq. (2)**. [OH⁻] and [Mg²⁺] are the molar concentrations of OH⁻ and Mg²⁺ ions respectively (mol m⁻³), j_{app} is the applied current density (A m⁻²), F is the Faraday constant (96485 C mol⁻¹), CE_{O_2} and CE_{H_2O} are the current efficiencies attributed to faradaic reactions (**Eq. (1)** and **Eq. (2)**). Following the methods adopted in our previous work [46], under the polarization of 4 mA cm⁻², their values were taken as 0, 0.0300, 0.0225, 0.0200, 0.0075 and 0.0050 % for CE_{O_2} and 0, 99.9700, 99.9775, 99.9800, 99.9925 and 99.9950% for CE_{H_2O} in respective order of 50, 100, 250, 500, 1000 and 3000 μm. Varying CE_{O_2} ascribed varying proportion of dissolved O₂ reduction into OH⁻ (**Eq. (7)**) on cathode surface including those produced from water oxidation on anode (**Eq. (8)**).



CE_{H_2} is the proportion of faradic current spent towards the concurrent H₂ evolution in **Eq. (2)** on cathode surface. The indirect contribution of HER towards the electro-precipitation kinetics was introduced through a term denoted as gas hindrance factor (α) due to H₂ gas bubbles and is defined in **Eq. (9)**:

$$\alpha = \nu_{\text{H}_2\text{O}} \frac{CE_{\text{H}_2\text{O}}}{n_{\text{H}_2\text{O}}} - \nu_{\text{H}_2} \frac{CE_{\text{H}_2}}{n_{\text{H}_2}} \quad (9)$$

Equation (7) can then be simplified into **Eq. (10)**:

$$r_{\text{OH}^-} = + \frac{d[\text{OH}^-]}{dt} = \frac{\nu_{\text{O}_2} j_{\text{app}}}{n_{\text{O}_2} F} CE_{\text{O}_2} + \alpha \frac{j_{\text{app}}}{F} \quad (10)$$

The rate of precipitation of $\text{Mg}(\text{OH})_2$ ($r_{\text{Mg}(\text{OH})_2}$) was estimated via **Eq. (11)**:

$$r_{\text{Mg}^{2+}} = -r_{\text{Mg}(\text{OH})_2} = -(k_{\text{Mg}(\text{OH})_2} + k_{\text{det,Mg}(\text{OH})_2})[\text{Mg}^{2+}][\text{OH}^-]^2 \quad (11)$$

where $r_{\text{Mg}^{2+}}$ is the heterogeneous rate of Mg^{2+} precipitation ($\text{mol m}^{-2} \text{min}^{-1}$), $k_{\text{Mg}(\text{OH})_2}$ is the third order rate constant associated to the reaction of electro-precipitation of $\text{Mg}(\text{OH})_2$ ($0.33 \text{ m}^7 \text{mol}^{-2} \text{min}^{-1}$ [46]) on cathode surface and $k_{\text{det,Mg}(\text{OH})_2}$ (in $\text{m}^7 \text{mol}^{-2} \text{min}^{-1}$) is the detachment rate constant of $\text{Mg}(\text{OH})_2$ due to gas evolution.

Since the precipitation of $\text{Mg}(\text{OH})_2$ consumed OH^- ions, its rate of reaction was accounted for in **Eq. (10)** and it can be written as **Eq. (12)**:

$$r_{\text{OH}^-} = + \frac{d[\text{OH}^-]}{dt} = \frac{\nu_{\text{O}_2} j_{\text{app}}}{n_{\text{O}_2} F} CE_{\text{O}_2} + \alpha \frac{j_{\text{app}}}{F} - 2(k_{\text{Mg}(\text{OH})_2} + k_{\text{det,Mg}(\text{OH})_2})[\text{Mg}^{2+}][\text{OH}^-]^2 \quad (12)$$

The electro-precipitation of CaCO_3 was modeled as function of the theoretical concentration of interfacial carbonates $[\text{CO}_3^{2-}]_{\text{int}}$ (in mol m^{-3}) (**Eq. (13)**) [46]:

$$[\text{CO}_3^{2-}]_{\text{int,t}} = \frac{K_{\text{A2}} \times \text{TIC}_t}{\frac{K_{\text{W}}}{[\text{OH}^-]_t} + K_{\text{A2}}} \quad (13)$$

where K_{A2} is the acidity constant of bicarbonate (HCO_3^-) / carbonate (CO_3^{2-}) acid-base couple ($pK_{\text{A2}} = 10.4$ [56]) and TIC_t is the evolution of concentration in the bulk of total inorganic carbons

($[\text{HCO}_3^-] + [\text{CO}_3^{2-}]$, without considering carbonic acid given the range of investigated pH) (mol m^{-3}). The modeled interfacial CO_3^{2-} (Eq. (13)) was dependent on the evolution of TIC_t in the bulk. They were assumed to be rapidly converted into CO_3^{2-} given the fact that the theoretical cathodic local pH (>11) was higher than pK_{A2} (10.4). Hence, the rate of precipitation of CaCO_3 (r_{CaCO_3}) was modeled by its kinetic law expressed in Eq. (14):

$$r_{\text{Ca}^{2+}} = -r_{\text{CaCO}_3} = -(k_{\text{CaCO}_3} + k_{\text{det,CaCO}_3}) [\text{Ca}^{2+}][\text{CO}_3^{2-}]_{\text{int}} \quad (14)$$

where $r_{\text{Ca}^{2+}}$ is the rate of heterogeneous Ca^{2+} precipitation ($\text{mol m}^{-2} \text{ min}^{-1}$), $[\text{Ca}^{2+}]$ is the molar concentration of Ca^{2+} (mol m^{-3}), k_{CaCO_3} is the second order rate constant of heterogeneous electro-precipitation of CaCO_3 ($3.6 \times 10^{-3} \text{ m}^4 \text{ mol}^{-1} \text{ min}^{-1}$ [46]) and $k_{\text{det,CaCO}_3}$ is the CaCO_3 detachment rate constant in $\text{m}^4 \text{ mol}^{-1} \text{ min}^{-1}$ due to concomitant evolving gas.

3.2. Relationship between double layer capacitance, double layer thickness and interelectrode distance

The double layer capacitance (C_{DL}) can be expressed in terms of the thickness of electronic double layer (d_{DL}) by Eq. (15) [57, 58]:

$$C_{\text{DL}} = \frac{\varepsilon_s \varepsilon_0}{d_{\text{DL}}} \quad (15)$$

where C_{DL} is expressed in F, ε_s the dielectric constant of solvent in bulk (here water, the value was taken at 80 [59-61]), ε_0 the vacuum permittivity ($8.854 \times 10^{-12} \text{ F.m}$ [60, 62]) and d_{DL} is expressed in m.

It is newly proposed to relate d_{elec} with d_{DL} , by assuming a proportionality relation using the following expression of Eq. (16):

$$d_{\text{elec}} = k (d_{\text{DL,A}} + d_{\text{DL,C}}) \quad (16)$$

where k is a constant ($k \gg 1$), $d_{DL,A}$ and $d_{DL,C}$ are the double layer thicknesses on anode and cathode respectively. Supposing the double layer thickness is identical on both anode and cathode ($d_{DL,A} = d_{DL,C}$), **Eq. (16)** is simplified into **Eq. (17)** and then into **Eq. (18)**.

$$d_{elec} = 2 k d_{DL} \quad (17)$$

$$d_{DL} = d_{elec}/(2k) \quad (18)$$

Inserting the expression of d_{DL} from **Eq. (18)** into **Eq. (15)** gives out a novel equation (**Eq. (19)**):

$$C_{DL} = \frac{\varepsilon_S \varepsilon_0 2 k}{d_{elec}} \quad (19)$$

3.3. Modeling software and fitting evaluation

The modeling of the evolution of Mg^{2+} and Ca^{2+} concentrations were done using Aquasim® software [63]. The calibration of the model was done with k_{det} , which was the only modeling parameter used to adjust the model to fit the experimental data (i.e., Ca^{2+} and Mg^{2+} concentrations evolution with electrolysis time and at varying d_{elec}). The fitting between experimental data and the kinetic models was evaluated using root mean square error (RMSE) (**Eq. (20)**) as well as model efficiency (ME) (**Eq. (21)**) [64]:

$$RMSE = \sqrt{\frac{\sum_{i=1}^K (y_i - y'_i)^2}{K}} \quad (20)$$

$$ME = 1 - \frac{\sum_{i=1}^K (y_i - y'_i)^2}{\sum_{i=1}^K (y_i - y_M)^2} \quad (21)$$

where y'_i the experimental value, y_i the model value, y_M is the average modeled value and K is the number of iterated values.

4. Results and discussion

4.1. Kinetics and modeling of mineral electro-precipitation at various interelectrode distances

The evolution of concentrations of Mg^{2+} , Ca^{2+} and TIC at different d_{elec} are illustrated in **Fig. 1**. From **Fig. 1(a)**, the electro-precipitation of $\text{Mg}(\text{OH})_2$ varied insignificantly with varying d_{elec} . The Mg^{2+} in the electrolyte precipitated by 85.7 ± 2.6 , 91.0 ± 0.2 , 91.2 ± 1.8 , 87.7 ± 0.9 and $89.2 \pm 4.2\%$ after 5-hour electrolysis for d_{elec} of 100, 250, 500, 1000 and 3000 μm respectively. **Figures 1(b) and 1(c)** plot the evolution of Ca^{2+} and TIC concentrations respectively, across multiple d_{elec} investigated. It can be observed that the CaCO_3 electro-precipitated the most at 100 μm and lesser precipitation of CaCO_3 was obtained with increasing d_{elec} (**Fig. 1(b)** and **Fig. 1(c)**). 55.1 ± 2.2 and $94.8 \pm 1.6\%$ of Ca^{2+} and TIC, respectively, were deposited on cathode using 100 μm . These percentages of precipitation decreased to 36.2 ± 5.6 and $82.1 \pm 0.9\%$ of Ca^{2+} and TIC, respectively, when the electrochemical cell was equipped with 3000 μm d_{elec} . Interestingly, it was noticed that there were no mineral electro-precipitation of $\text{Mg}(\text{OH})_2$ and CaCO_3 at the lowest d_{elec} investigated (50 μm) (**Fig. 1**). These results suggested that the mineral electro-precipitation, particularly CaCO_3 , tended to occur easier when shifting progressively from millimetric into microfluidic setup, except at the lowest d_{elec} investigated (50 μm).

The Mg and Ca mass balances recovery have been estimated to ensure that not only there was no loss of electrolyte during electrolysis (i.e., via leakage or dead volume in the pilot), but also to verify that the trend of the occurrence of mineral cathodic deposition was correct. **Figure S1** shows the mass balances of Mg and Ca successively recovered from different parts of experimental pilot after 5 h of electrolysis under all investigated d_{elec} . The sum of the remaining Mg and Ca in solution with their mass recovered from anode, cathode and tubing remained above $84 \pm 5\%$ with the average recovery of $91.2 \pm 2.2\%$ for Mg and $99.7 \pm 4.1\%$ for Ca across all d_{elec} investigated. The majority of Mg and Ca precipitated from electrolyte was found on cathode, while little mass was recovered from tubing and anode surface. This observation can confirm the cathodic precipitation of

Mg(OH)₂ and CaCO₃ induced by the phenomenon of local alkalization on cathode surface [1, 2, 65] and validate the results presented in Fig. 1.

As can be observed in Fig. 1, the model curves of Mg²⁺, Ca²⁺ and TIC fitted well with their experimental counterparts at different d_{elec} under study, which confirmed the need to consider gas bubbles evolution through α and scale detachment parameters as discussed in Section 4.2. The calculated RMSE values for Mg²⁺, Ca²⁺ and TIC curves fitting across all d_{elec} are tabulated in Table S3. RMSE values for Mg²⁺ curves fitting was as low as 0.0037 under 3000 μm configuration, whilst the highest error (0.0109) was found under the 250 μm setup (Table S3). The lowest and highest RMSE values in Ca²⁺ curves fitting were 0.0784 and 0.1435, corresponding to d_{elec} of 250 μm and 100 μm respectively. The kinetics of TIC evolution in the bulk under all d_{elec} were pseudo first-order rates, as already previously noticed [46]. The lowest RMSE (0.0818) was found for 50 μm , whereas the highest RMSE (0.4658) corresponded to the configuration of 500 μm .

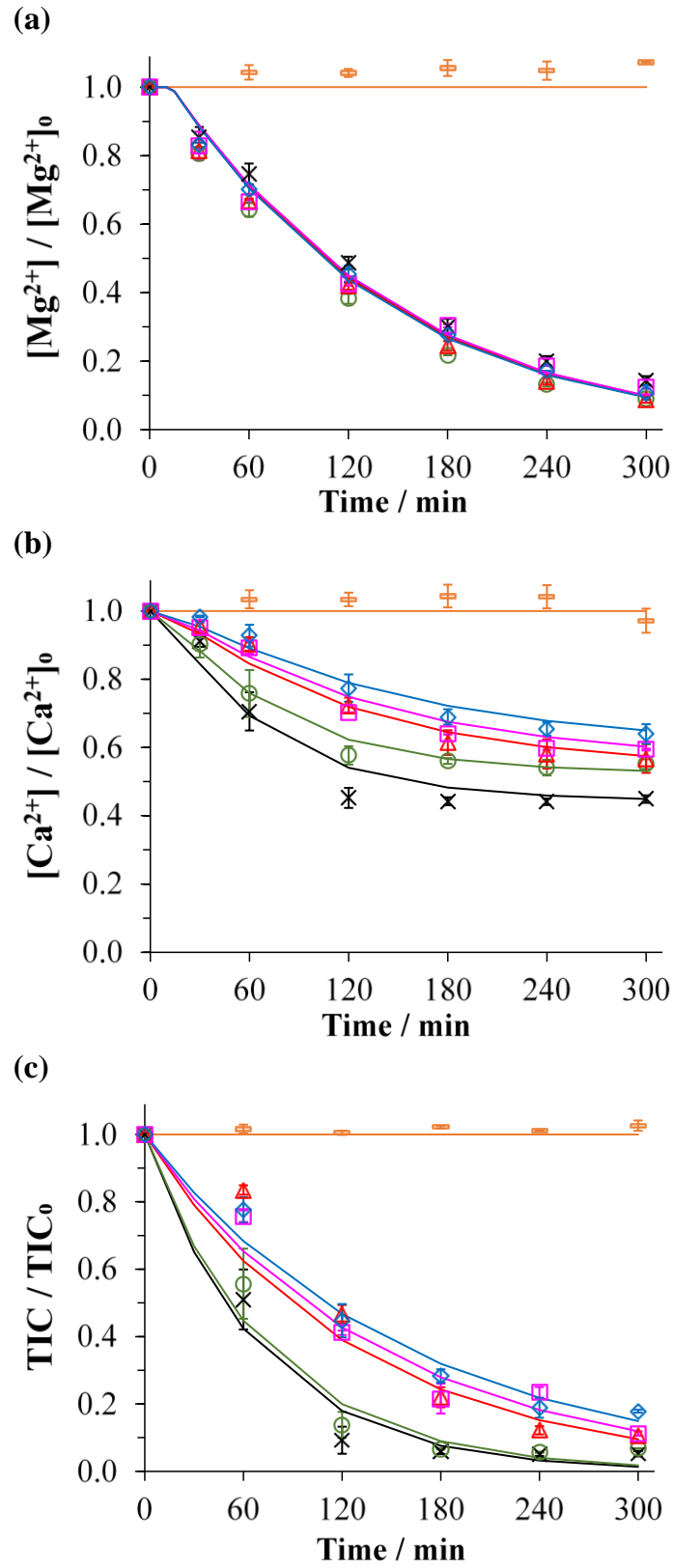


Fig. 1. Evolution of experimental and modeled concentrations of Mg^{2+} , Ca^{2+} and TIC during the electrolysis at 4 mA cm^{-2} for different d_{elec} (—: $50 \mu\text{m}$, \times : $100 \mu\text{m}$, \circ : $250 \mu\text{m}$, \triangle : $500 \mu\text{m}$, \square :

1000 μm and \diamond : 3000 μm). Cathode: SS and anode: BDD. Solution containing 150 mg L^{-1} of Ca^{2+} , 5 mg L^{-1} of Mg^{2+} and 60 mg L^{-1} of TIC.

4.2. Impact of cathode potential on mineral electro-precipitation at different interelectrode distances

The trends observed in [Section 4.1](#) can be elucidated by the values of cathode potential (E_C) measured using the potentiostat, when 4 mA cm^{-2} current density was applied to the different electrochemical cell configurations. E_C values along with the average percentages of mass of Mg, Ca and TIC electro-precipitated after 5 h of electrolysis at 4 mA cm^{-2} for each d_{elec} are illustrated in [Fig. 2\(a\)](#). It can be noticed that the E_C values dropped significantly from 0.202 ± 0.024 V/Ag-AgCl (50 μm) to -1.453 ± 0.021 V/Ag-AgCl (100 μm). The diminishing trend continued further down to -1.915 ± 0.030 V/Ag-AgCl when 3000 μm was equipped. LSV curves corresponding to all investigated d_{elec} are presented in [Fig. S2](#). Across all interelectrode gaps, the plateau of limiting current of reduction of dissolved O_2 into OH^- ions ([Eq. \(1\)](#)) were noticeable in the potential range of -0.7 to -1.10 V/Ag-AgCl ([Fig. S2](#)). Comparable range of values have been reported in literature [\[27, 32, 36-38, 47, 49\]](#). Within these ranges of applied potential, OH^- production via 4-electron of dissolved O_2 reduction reaction (ORR) was the most selective with minimal concomitant gas evolution on electrodes surface. The E_C measured with 100 μm (-1.453 ± 0.021 V/Ag-AgCl) was the closest to the potential of ORR into OH^- (-0.7 to -1.10 V/Ag-AgCl). As a consequence, amongst the various d_{elec} under study, the electro-precipitation of $\text{Mg}(\text{OH})_2$ ([Eq. \(3\)](#)) and CaCO_3 ([Eq. \(6\)](#)) took place with minimal evolving H_2 perturbation when the electrochemical cell was equipped with 100 μm . As the d_{elec} increased, E_C progressively moved farther away into the region of potential of H_2O reduction which started at about -1.10 V/Ag-AgCl according to [Fig. S2](#). Within this region, the OH^- production still occurred but concomitantly with HER [\[25, 47-49, 66-68\]](#). As a result, lesser production of mineral electro-precipitation was observed with the increasing interelectrode gap. Furthermore, using the LSV curves plotted in [Fig. S2](#), Tafel slopes [\[69, 70\]](#) corresponding to the

region of measured E_C for all d_{elec} configurations were determined and they are illustrated in **Fig. 3**. Tafel slope corresponding to d_{elec} of 3000 μm depicted the highest slope (-1.57 V dec^{-1}) amongst all the investigated d_{elec} , which accentuated the fact that the highest overpotential was obtained while operating with 3000 μm in comparison with the micrometric distances (-0.38 V dec^{-1} using 100 μm).

The higher concurrent H_2 evolution activity when d_{elec} increased can be further justified by the ratio of initial limiting current densities ($j_{\text{lim},0}$) over the current density adopted (j_{app}). The values of $j_{\text{lim},0}$ were calculated using **Eq. (S1)** for different d_{elec} configurations **[51]** and are plotted in **Fig. 2(b)**. When the j_{app} value is inferior or equal to $j_{\text{lim},0}$ (i.e. $j_{\text{lim},0}/j_{\text{app}} \geq 1$), it represents a condition in which OH^- is produced from the 4-electron ORR of **Eq. (1)** without any parasitic HER (**Eq. (2)**) **[71, 72]**. When j_{app} was greater than $j_{\text{lim},0}$ ($j_{\text{lim},0}/j_{\text{app}} < 1$), it means that OH^- production was accompanied by concomitant HER due to mass transfer limitation of dissolved O_2 . From **Fig. 2(b)**, it can be observed that the $j_{\text{lim},0}$ values decreased when d_{elec} increased. Hence, the $j_{\text{lim},0}/j_{\text{app}}$ was further reduced with increasing d_{elec} and remained below 1 whatever the distance (**Table S1**). Consequently, parasitic HER was more pronounced with increasing d_{elec} . Contrastingly, under the 50 μm d_{elec} setup, the E_C measured was too high for the 4-electron ORR yet to occur. As a result, neither reduction of dissolved O_2 ($CE_{\text{O}_2} = 0$) nor water ($CE_{\text{H}_2\text{O}} = 0$) took place. Hence, $r_{\text{OH}^-} = 0$ (**Eq. (12)**). Consequently, $r_{\text{Mg}^{2+}}$ (**Eq. (11)**) and $r_{\text{Ca}^{2+}}$ (**Eq. (14)**) were both nil. This enlightened the reason why no precipitation was spotted at this minimum d_{elec} investigated. Whereas, using other investigated d_{elec} , the OH^- production occurred moreover with increasing HER intensity when d_{elec} increased. These phenomena were accounted for during the modeling of Mg^{2+} and Ca^{2+} concentrations via α and k_{det} parameters in **Eqs. (9), (11), (12) and (14)**. α values in **Eq. (9)** were estimated from CE_{O_2} and $CE_{\text{H}_2\text{O}}$ obtained experimentally. CE_{H_2} was assumed to be equal to $CE_{\text{H}_2\text{O}}$, since they belong to the same half-equation (**Eq. (2)**). As a result, α in **Eq. (12)** took values of 0, 0.49985, 0.49989, 0.49990, 0.49996 and 0.49998 for d_{elec} of 50, 100, 250, 500, 1000 and 3000 μm ,

respectively. α increased with increasing d_{elec} because of the increasing hindrance of precipitating ions to reach cathode surface due to increasing H_2 evolution intensity. $k_{\text{det,CaCO}_3}$ (in Eq. (14)) and $k_{\text{det,Mg(OH)}_2}$ (in Eq. (11)) were the only fitted parameters to match the experimental curves of Ca^{2+} and Mg^{2+} at different investigated interelectrode gaps (Fig. 1). $k_{\text{det,CaCO}_3}$ increased from 0.1, 1.0, 2.3, 2.5 to $2.75 \times 10^{-3} \text{ m}^4 \text{ mol}^{-1} \text{ min}^{-1}$ using d_{elec} of 100, 250, 500, 1000 and 3000 μm , respectively. It suggested that more CaCO_3 detachment occurred with the more vigorous HER in ascending order of d_{elec} . Meanwhile, $k_{\text{det,Mg(OH)}_2}$ was fitted at $1 \times 10^{-3} \text{ m}^7 \text{ mol}^{-2} \text{ min}^{-1}$ for all d_{elec} except 50 μm (no deposition), since the electro-precipitation of Mg(OH)_2 was independent of d_{elec} (Fig. 1). It could be explained by the lower solubility constant of Mg(OH)_2 (10^{-12} [73, 74]) in comparison with the one of CaCO_3 (10^{-9} [74-77]). It means that Mg(OH)_2 could precipitate easier compared to CaCO_3 . It precipitated as soon as the interfacial pH reached 10.2 according to our previous work [46]. The theoretical interfacial pH of 10.2 was quickly attained, i.e., after 14 min of electrolysis and it increased up to 11.6 during the process [46]. Owing to this alkaline environment and to the fact that the Mg(OH)_2 precipitation involved direct reaction of Mg^{2+} with OH^- , the detached Mg(OH)_2 would easily precipitate back on cathode surface, unlike CaCO_3 . Therefore, the Mg(OH)_2 deposition varied negligibly as function of d_{elec} .

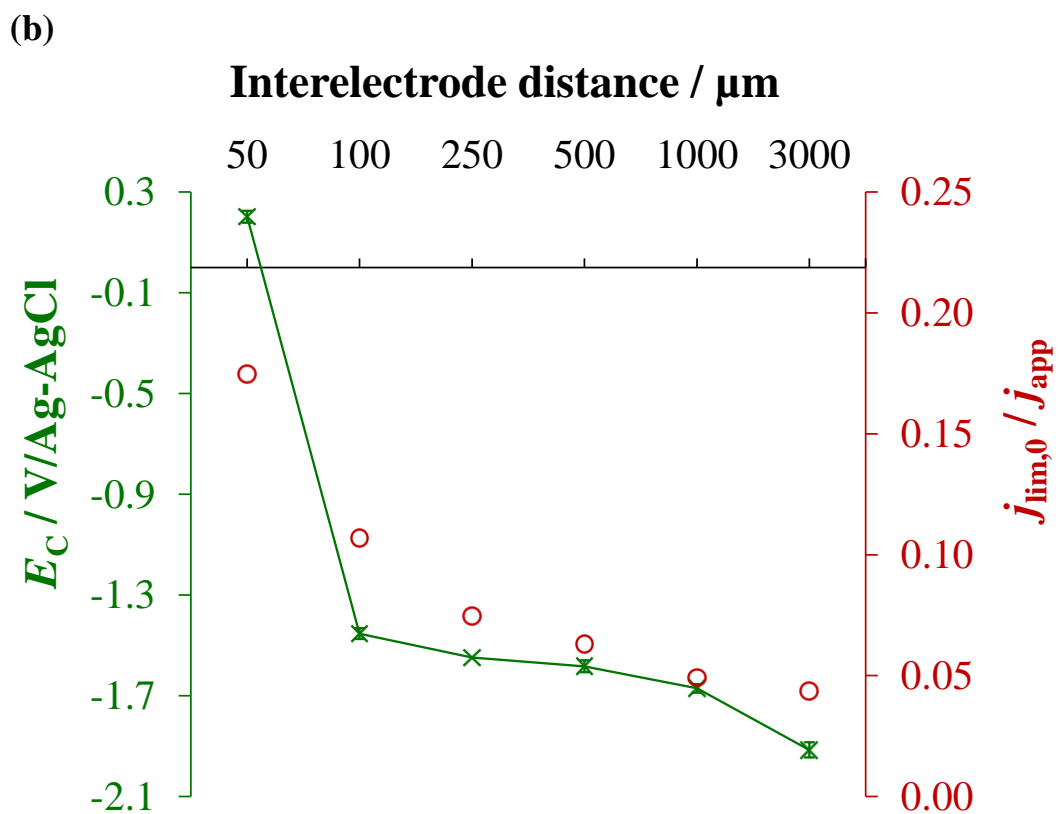
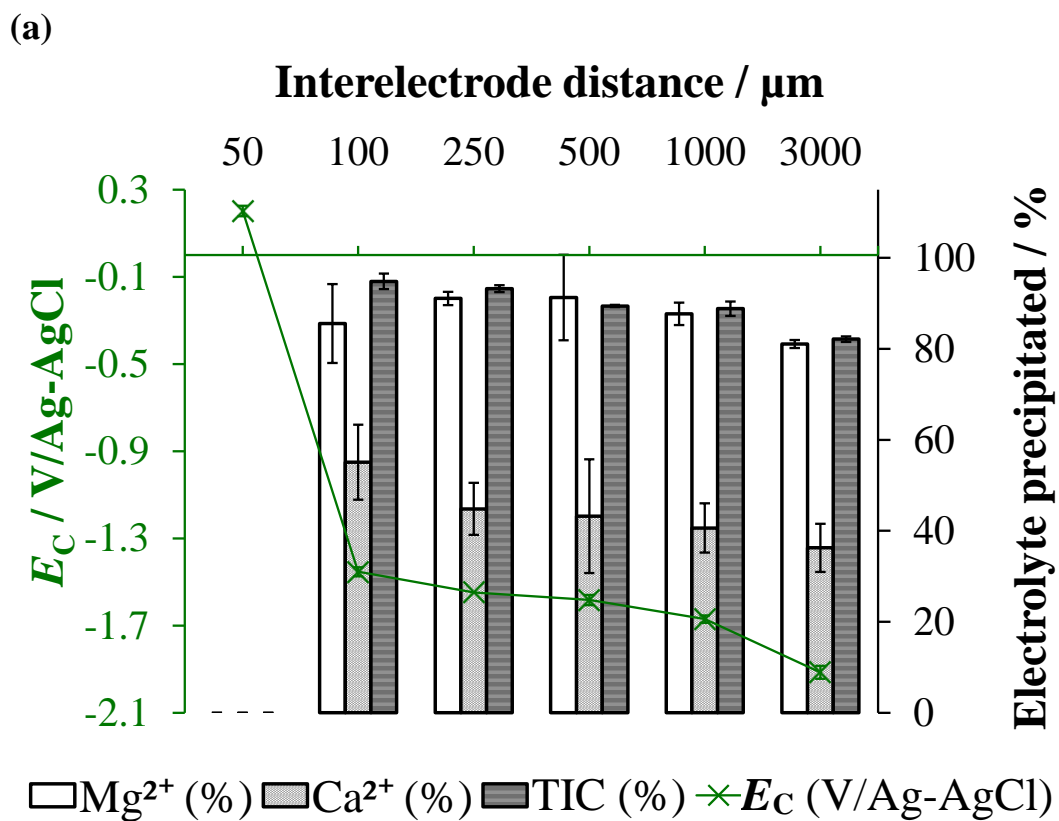


Fig. 2. Influence of d_{elec} on the evolution of (a) E_C (×) and average percentage of Mg (□), Ca (◐) and TIC (◑) electro-precipitated, and (b) $j_{\text{lim},0}/j_{\text{app}}$ (○). Cathode: SS, anode: BDD, j_{app} : 4 mA cm^{-2} . Solution contained 150 mg L^{-1} of Ca^{2+} , 5 mg L^{-1} of Mg^{2+} and 60 mg-C L^{-1} of TIC.

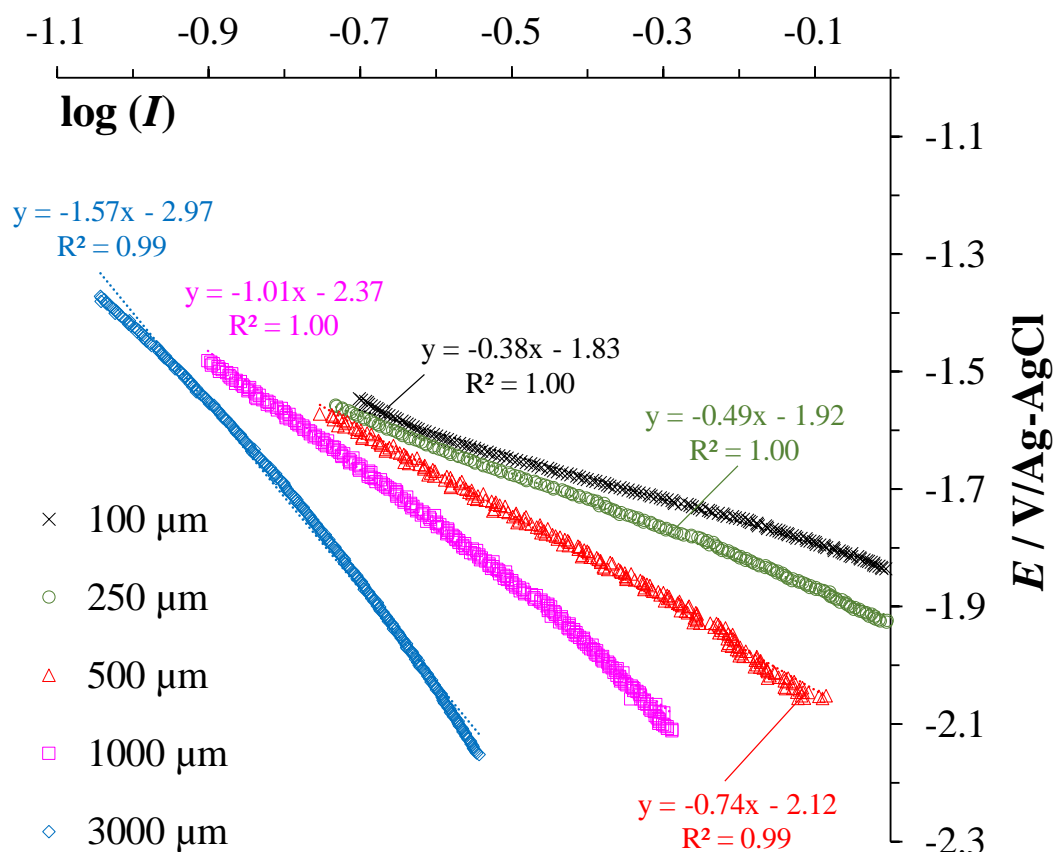


Fig. 3. Tafel slopes in the range of investigated j_{app} (4 mA cm^{-2}) across different d_{elec} configurations. Solution contained 150 mg L^{-1} of Ca^{2+} , 5 mg L^{-1} of Mg^{2+} and 60 mg-C L^{-1} of TIC.

Working electrode (cathode): SS and counter electrode (anode): BDD.

4.3. Contribution of dissolved O_2 from anodic oxidation in microfluidic versus millimetric electrochemical reactors

To further affirm the role of E_C in the occurrence of electro-precipitation at different d_{elec} , experiments were performed in potentiostatic mode at identical E_C (-1.6 V/Ag-AgCl) - the applied E_C measured on cathode when 4 mA cm^{-2} was applied under $500 \mu\text{m}$ setup - for 500 and $3000 \mu\text{m}$ interelectrode gaps. The electrolyte contained 150 mg L^{-1} of Ca^{2+} , 5 mg L^{-1} of Mg^{2+} and 60 mg L^{-1} of TIC, similar to that used in Fig. 2. The resulting evolution of Mg^{2+} , Ca^{2+} and TIC concentrations under the potentiostatic electrolysis are given in Fig. 4. It was observed that after 5 h of electrolysis, $85.2 \pm 4.0\%$ of Mg^{2+} precipitated on cathode under submillimetric setup whereas only $59.2 \pm 1.8\%$

of Mg^{2+} from electrolyte was deposited under millimetric setup (**Fig. 4(a)**). At the end of the electrolysis, it was noticed a similar amount of Ca^{2+} deposited using 500 μm ($50.6 \pm 0.1\%$) in comparison with 3000 μm ($49.4 \pm 1.2\%$) with however slightly faster kinetics of Ca^{2+} precipitation under microfluidic configuration up till 4 h of electrolysis (**Fig. 4(b)**). The TIC evolution in **Fig. 4(c)** suggested that faster consumption of carbonates species occurred under microfluidic setup leading to $93.5 \pm 0.3\%$ of CO_3^{2-} precipitated with Ca^{2+} forming CaCO_3 at 500 μm against $89.0 \pm 1.3\%$ of CO_3^{2-} precipitation occurring at 3000 μm . The difference of electro-precipitation observed at both distances and at the same applied E_C indicated that E_C was not the sole influencing factor. The influence of the electrochemical reactor geometry could be also involved. The dissimilarity observed in **Fig. 4** could then confirm the difference that could have been brought while transitioning into the microfluidic configuration. Using micrometric d_{elec} , the rate of OH^- production in **Eq. (12)** was intensified by external provision of dissolved O_2 coming from the oxidation of solvent on anode (**Eq. (8)**), producing more OH^- in comparison to the millimetric d_{elec} . The OH^- production was limited by mass transport of dissolved O_2 [47, 78]. Hence an increase in dissolved O_2 concentration at the locality of cathode surface would increase the OH^- production. Consequently, interfacial OH^- concentration was higher under microfluidic than millimetric setup. Subsequently, thermodynamics of **Eq. (3)** and **Eq. (5)** were shifted to the right to favor the precipitation reaction of $\text{Mg}(\text{OH})_2$ and the production of CO_3^{2-} respectively. Therefore, quicker kinetics and more electro-precipitation of $\text{Mg}(\text{OH})_2$ and CaCO_3 perceived in **Fig. 4** at identical applied E_C are justified. This anodic provision of dissolved O_2 could also occur using 3000 μm as well, but it did at much lesser extent. This deduction justified the higher evaluated CE_{O_2} when 100 μm d_{elec} (0.03%) was equipped compared to using 3000 μm (0.005%) d_{elec} . One could question that the production of protons in **Eq. (8)** could compensate in the meantime the interfacial OH^- at cathode vicinity under microfluidic configuration to produce H_2O (**Eq. (22)**), which could however be reduced back to OH^- in agreement with **Eq. (2)**.



From a practical point of view, it was noticed that within the case where no mineral precipitation was observed, for example, using 50 μm d_{elec} , the bulk pH tended to increase (**Fig. S3**). This feature was also observed in the previous work when the operating conditions allow avoiding electro-precipitation using 500 μm interelectrode gap [46]. This shows that the intensification of OH^- production due to the anodic source of dissolved O_2 was more predominant than the compensation of protons with OH^- , at both interface and in the bulk.

With regard to the use of BDD anode, it is worth mentioning that, physisorbed hydroxyl radicals ($\bullet\text{OH}$) could be produced upon reaching its redox standard potential of 2.7 – 2.8 V versus standard hydrogen potential (SHE) [9, 79]. When the electrochemical cell worked with 500 and 3000 μm d_{elec} , under the polarization of 4 mA cm^{-2} , the anode potentials were 2.65 and 3.41 V/SHE respectively. In these conditions, it could be possible that the production of $\bullet\text{OH}$ might be more preferable over O_2 evolution using BDD anode. Consequently, lesser provision of dissolved O_2 from anode might be possible. Since anode potential increased with d_{elec} , the contribution from anodic dissolved O_2 at cathode would even decrease further when d_{elec} decrease.

Again, in term of practicability, electrolysis in galvanostatic mode has more interest for the application in the real field. The incoming sections are devoted to further enlighten the mechanism of mineral scaling evolution at different d_{elec} by exploiting the concomitant gas evolution and characterizing the electrode/electrolyte interface through impedance studies.

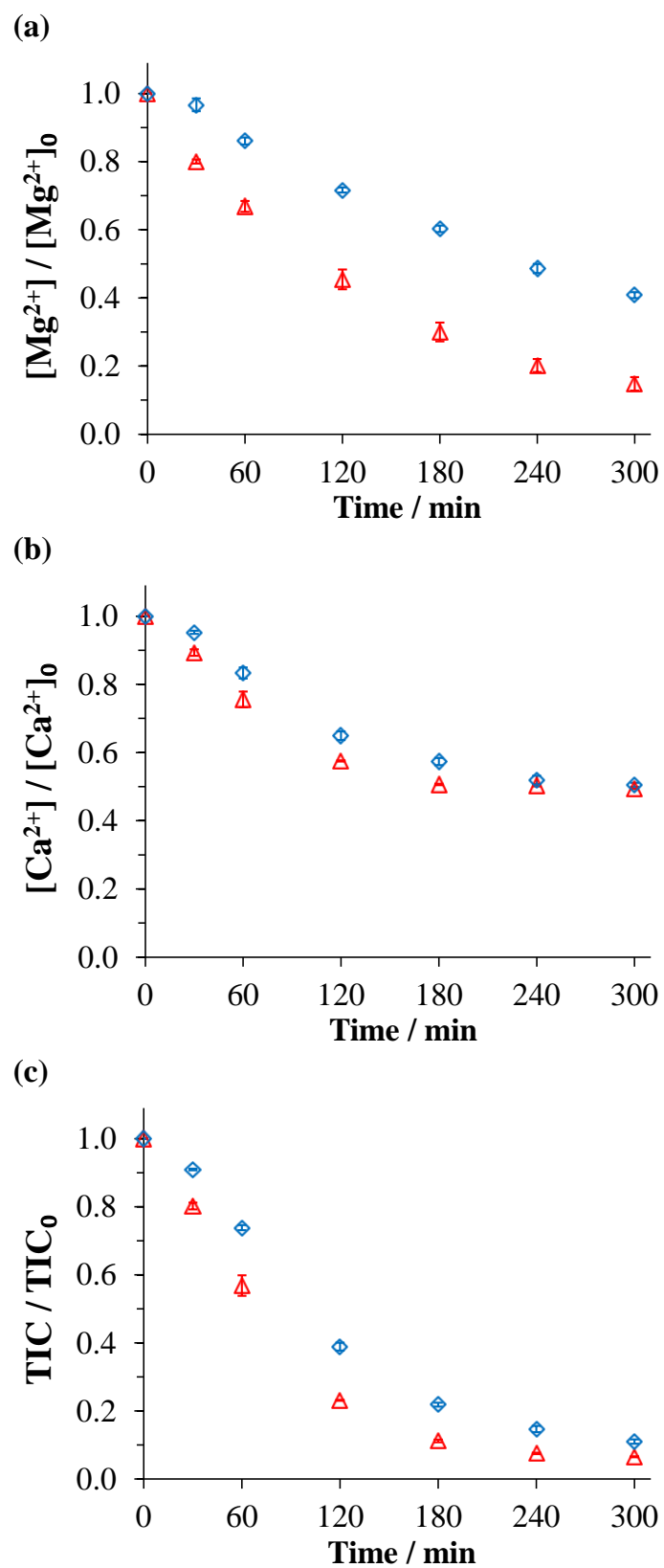


Fig. 4. Evolution of Mg^{2+} , Ca^{2+} and TIC concentrations during the electrolysis of solution containing 150 mg L^{-1} of Ca^{2+} , 5 mg L^{-1} of Mg^{2+} and 60 mg L^{-1} of TIC at constant E_C of -1.6 V/Ag-

AgCl under microfluidic (500 μm , \triangle) and millimetric (3000 μm , \diamond) configurations. Working electrode: SS and counter electrode: BDD.

4.4. The influence of gas evolution on the formation of mineral electro-precipitation

It has been shown that α and k_{det} parameters, accounting for physical gas evolution on cathode surface (Eqs. (9)-(14)), was primordial to yield reliable model fittings to the Mg^{2+} , Ca^{2+} and TIC experimental curves (Section 4.1). It was also demonstrated that the more d_{elec} increased, the more the ratio of $j_{\text{lim},0}/j_{\text{app}}$ decreased due to decreasing $j_{\text{lim},0}$ with increasing d_{elec} (Section 4.2). As a consequence, the secondary HER was more vigorous when the d_{elec} increased. Subsequently, the mineral electro-precipitation decreased with d_{elec} . This feature was also supported by the evolution of E_C values that decreased progressively farther into the region of water reduction with increasing d_{elec} (Fig. 2). This new interesting insight indicates the impactful influence that the gas evolution has on the formation of mineral electro-precipitation at various d_{elec} . Thus, it merits further in-depth investigations as discussed in this sub-section.

The evolution of reduced conductivity of electrolyte (κ/κ_0), which is the ratio of ionic conductivity of electrolyte containing dispersed gas bubbles (κ) over ionic conductivity of electrolyte free of gas bubbles (κ_0) [80], is plotted as function of time for different d_{elec} in Fig. 5(a). It has been noticed that κ/κ_0 decreased the most under the configuration of 100 μm , while it increased progressively with d_{elec} . Therefore, κ/κ_0 decreased the most under the configuration where the mineral electro-precipitation occurred the most (i.e., 100 μm), while when no mineral precipitation was observed (i.e., at 50 μm), κ/κ_0 remained constant over the course of electrolysis. Due to the non-conducting nature of gas bubbles [81, 82], the ionic conductivity of electrolyte is reduced. Using the experimental data of κ/κ_0 , the equation of Bruggeman written in Eq. (23) allows estimating the gas

void (φ) - the fraction of gas volume over the total volume of liquid and gas - for different d_{elec} at 4 mA cm⁻².

$$\varphi = 1 - \left(\frac{\kappa}{\kappa_0} \right)^{2/3} \quad (23)$$

The φ values are plotted against the interelectrode gap in **Fig. 5(b)**. φ was noticed to decrease as function of d_{elec} , which agreed with the above-mentioned trend of κ/κ_0 with d_{elec} (**Fig. 5(a)**). In microfluidic reactors, the concurrent gas evolution already took place inside the submillimetric volume. It means that the resistivity due to non-conducting gas bubbles was at the highest under the configuration of 100 μm and it decreased progressively in the increasing order of d_{elec} . The higher values of φ obtained in smaller interelectrode gaps was confirmed by several works in literature **[81, 83]**.

The term relative resistivity (ρ/ρ_0) (**Eq. (24)**) is also used in literature to depict the evolution of electrolyte resistivity, which is simply the inverse of κ/κ_0 . The ρ/ρ_0 is plotted as function of d_{elec} in **Fig. 5(b)**.

$$\frac{\rho}{\rho_0} = 1 / \left(\kappa / \kappa_0 \right) \quad (24)$$

ρ/ρ_0 decreased in the increasing order of d_{elec} . Comparable trend of the evolution of relative resistivity as function of interelectrode gap has also been highlighted from the work of Hine et al. **[84, 85]** and Vogt et al. **[86]** but in larger range of interelectrode gap (5 to 70 mm) and relatively larger applied current densities (75 to 375 mA cm⁻²).

In a nutshell, the relationship between the gas evolution, gas void as well as relative resistivity with the formation and possible detachment of mineral scaling on cathode surface at different interelectrode gaps can be schematized in **Fig. 6**. The least electro-deposition took place at the

highest d_{elec} under study (3000 μm) owing to vigorous evolving gas whilst the mineral scaling occurred the most under the 100 μm configuration.

The internal ohmic resistance ($\sum RI$) of an electrochemical cell not only varies with the variation of interelectrode gap but is also affected by the evolving gas bubbles which act as moving electrical insulators in-between electrodes [82]. Therefore, in quest to investigate the evolution of $\sum RI$ as function of d_{elec} , $\sum RI$ was evaluated by **Eq. (25)**.

$$\sum RI = \Delta U - |E_C| - |E_A| \quad (25)$$

where $\sum RI$ is the ohmic drop (V), ΔU is the cell voltage, $|E_C|$ and $|E_A|$ are the absolute values of cathode and anode potentials respectively.

The plot of $\sum RI$ and overall ΔU as function of d_{elec} are given in **Fig. 7**. It can be clearly observed that, as the d_{elec} decreased, the ohmic drop and cell voltage decreased linearly down to 100 μm . Interestingly, the decrease of $\sum RI$ occurred abruptly below 100 μm , breaking the linearity observed in the range of 100 μm to 3000 μm configuration. This is the first time that the non-linearity of ohmic resistance is assessed under the microfluidic setup unlike the linear decrease of $\sum RI$ usually observed using millimetric distances in literature (**Eq. (26)**) [87].

$$\sum RI = \frac{j_{\text{app}} d_{\text{elec}}}{\kappa_0} \quad (26)$$

In the presence of gas bubbles, **Eq. (26)** is slightly modified to take into consideration the gas void fraction as shown in **Eq. (27)** [84, 86]:

$$\sum RI = \frac{j_{\text{app}}}{\kappa_0 (1-\varphi)^{3/2}} d_{\text{elec}} \quad (27)$$

The slope value obtained from the linear trend in **Fig. 7**, for distances ranging from 100 to 3000 μm , equaled 0.2435 V mm^{-1} ($R^2 = 0.95$).

In conclusion, the ΣRI decreased with decreasing d_{elec} and higher φ fraction in submillimetric region made the ΣRI decrease non-linearly. A decrease in electrolytic ΣRI does indeed reduce the energy consumption of an EAOP, nevertheless it does not promise a decrease in mineral scaling formation as practically proven in this work. More mineral precipitation occurred, while the ΣRI decreased in descending order of d_{elec} down to 100 μm .

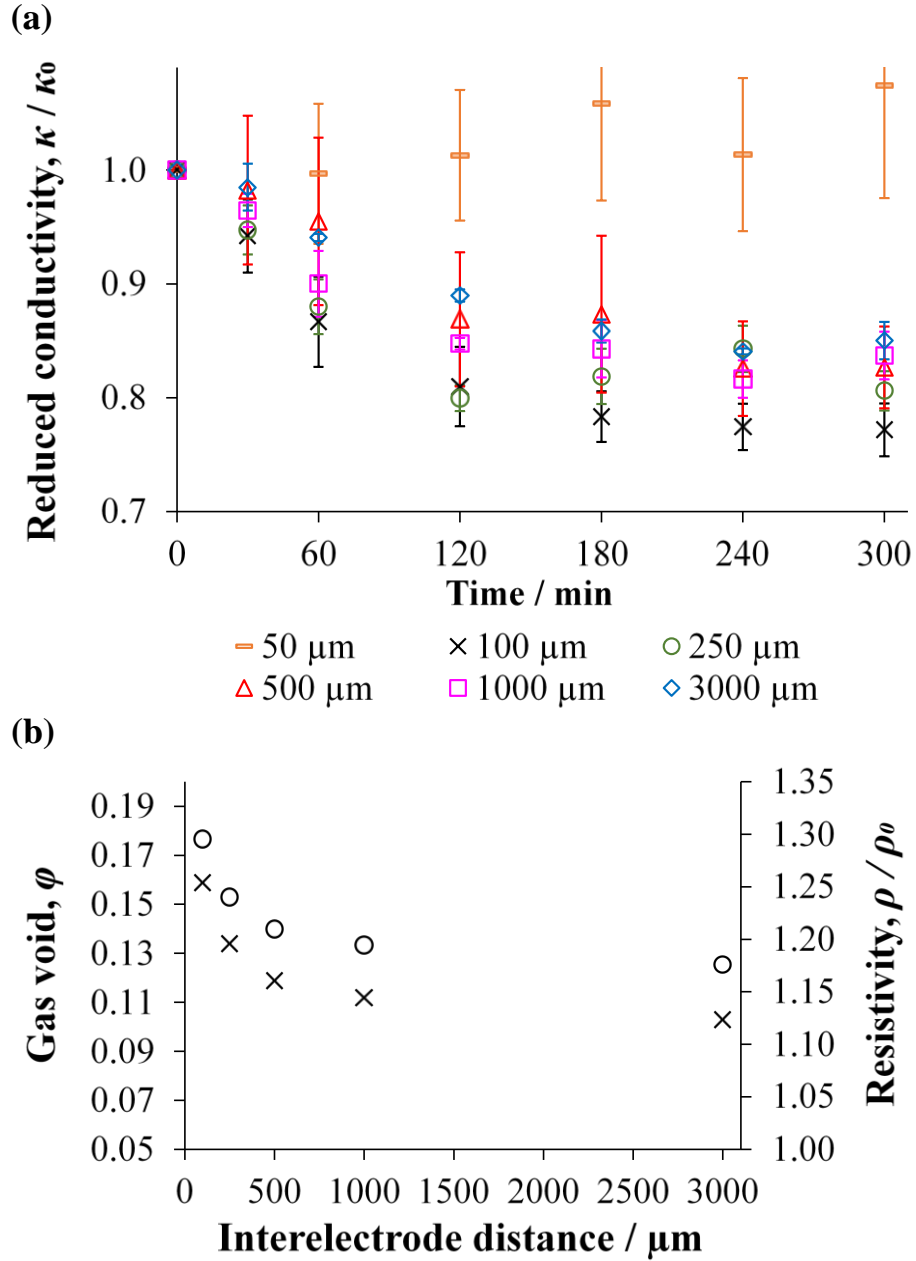


Fig. 5. (a) Evolution of κ/κ_0 of electrolyte in-between different d_{elec} and (b) influence of d_{elec} on the φ fraction (\times) and electrolyte resistivity ρ/ρ_0 (O). Cathode: SS, anode: BDD and $j_{\text{app}} = 4 \text{ mA cm}^{-2}$.

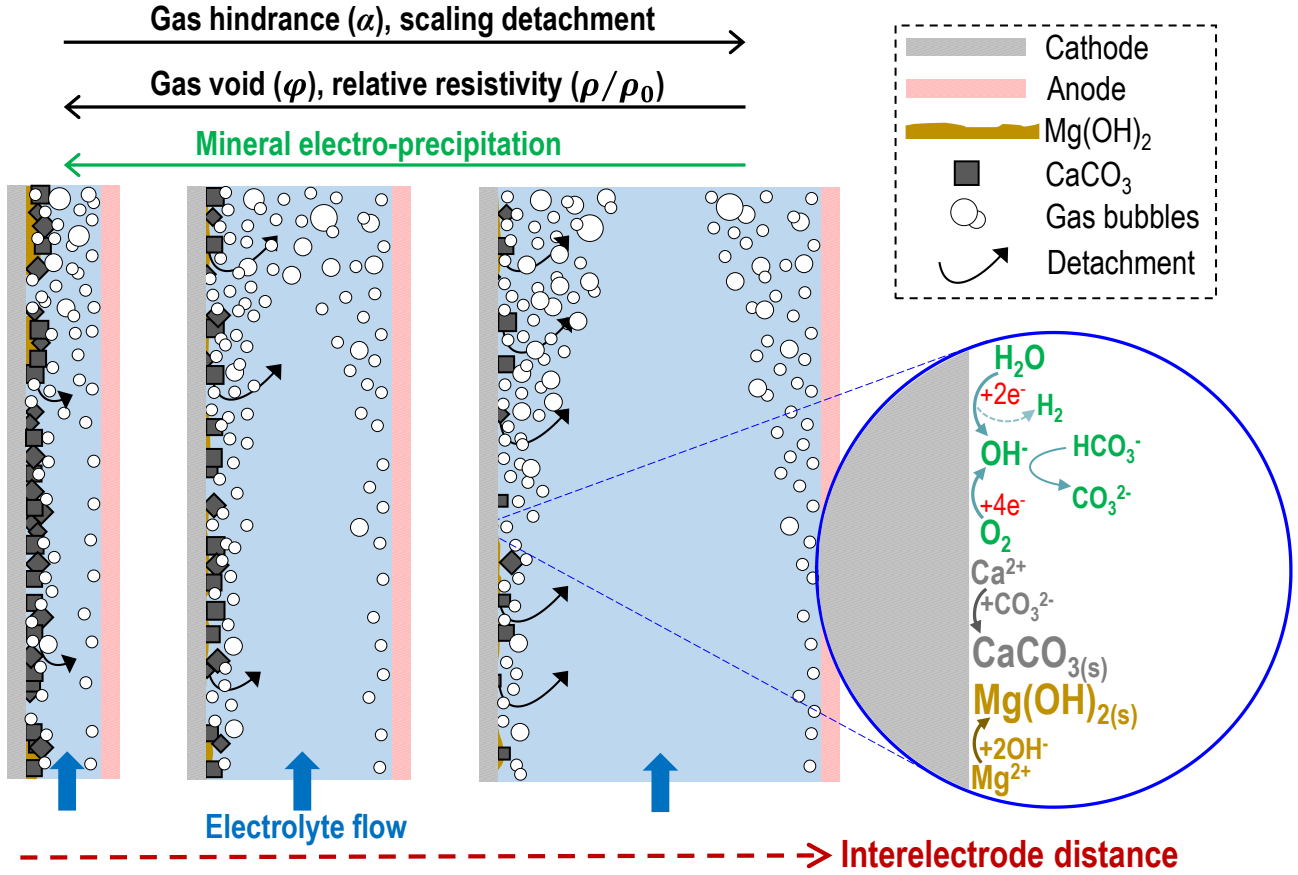


Fig. 6. Mechanistic scheme describing the relationship between mineral electro-precipitation with the occurring concurrent gas evolution on cathode surface under different d_{elec} configurations.

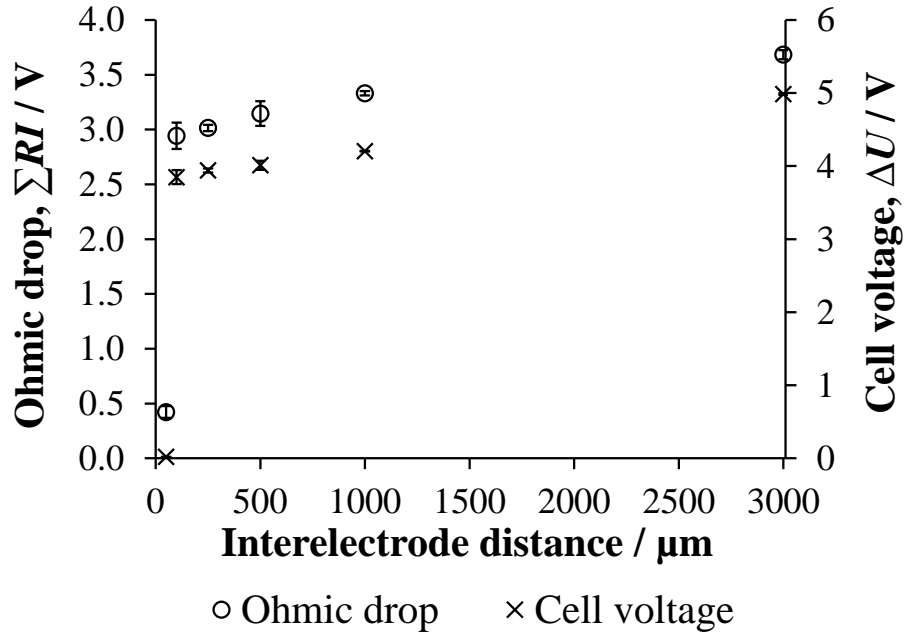


Fig. 7. Ohmic drop (ΣRI) of electrolyte (○) and cell voltage (ΔU) (×) as function of d_{elec} . Cathode:

SS, anode: BDD and $j_{\text{app}} = 4 \text{ mA cm}^{-2}$.

4.5. Cathode/electrolyte interface impedance study of electro-precipitation at different interelectrode distances

It is presented here-in for the first time, the interfacial parameters acquired by EIS analysis of a scalable electrochemical reactor in the aim at better understanding the cathode/electrolyte interface mechanism under electro-precipitation condition considering wide ranges of d_{elec} . The EIS extracted parameters under distinct configurations of millimetric into submillimetric setup are compared and discussed. A mechanistic scheme of mineral electro-precipitation on cathode surface is proposed with the integrated EEC to characterize the precipitation using EIS (Fig. 8). R_F and C_F corresponded respectively to the resistance and capacitance of porous non-conductive precipitation film. Charge transfer resistance (R_{CT}) was attributed to the difficulty of electronic transfer for electrochemical reactions to occur on cathode surface as the mineral electro-precipitation grew over time. R_{SOL} was attributed to the resistance of electronic transfer in electrolyte between cathode (as working electrode) and reference electrode. Instead of pure capacitor circuit element, constant phase element

(CPE_{DL}) was used to model the charging of non-faradaic capacitive electronic behavior that occurred on bare cathode surface - the area where there was no electro-precipitation - with ions present in electrolyte. This capacitive response was due to the electronic double-layer formed at the polarized interface. CPE_{DL} was more apt to account for not only the non-homogeneity of distribution of metallic elements that composed stainless steel cathode [88-90] but also non-ideality of capacitive response due to uneven coverage of porous electro-precipitation and evolving gas on cathode surface [37, 38, 91, 92]. The value of C_{DL} is linked with CPE_{DL} (in F) by Eq. (28) [89, 91-93]:

$$CPE_{DL} = C_{DL}^n [R_{SOL}^{-1} + R_{CT}^{-1}]^{(1-n)} \quad (28)$$

where n ($0 < n < 1$) is the constant phase element parameter and R_{SOL} as well as R_{CT} are expressed in Ohms.

Another time-constant, $L-R_{DES}$ (L in Henry and R_{DES} in Ohms) was added to complete the equivalent circuit. This pair of time constant is ascribed to R_i-C_i couple when R_i and C_i take negative values, as the outcome of mathematical fitting of equivalent circuit to experimental data. This is often used when induction loop appears in the experimental data, which was also noticed previously not only in batteries, fuel cells and corrosion study but also in water electrolysis system with gas evolving electrodes [94-98]. Consequently, the inductive loop in our experimental spectra has been attributed to the possible adsorption/desorption of mineral electro-precipitate at the cathode surface.

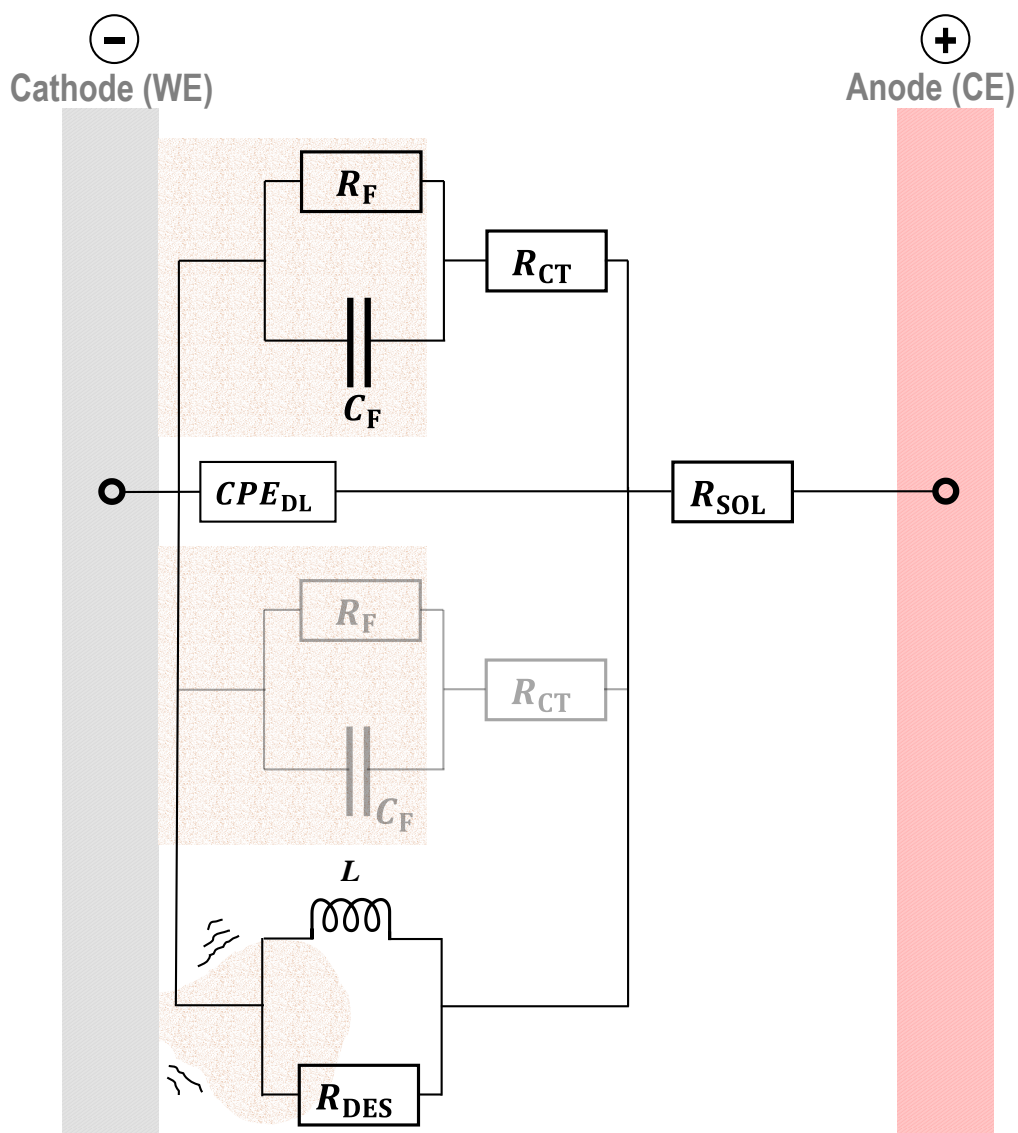


Fig. 8. Mechanistic scheme of mineral electro-precipitation on cathode surface including the representation of EEC used in EIS modeling. Working electrode: SS and counter electrode: BDD.

The validity of the impedance spectra obtained in our experiments was checked and validated by the linear Kramers-Kronig transform (KKT) method [99-104] and they were plotted against the experimental data at varying d_{elec} as shown in Fig. S4. The chi-squared residues (χ^2) between linear KKT and EEC model fitting curves against experimental data are tabulated in Table S4. The experimental curves complied well with the KKT plots considering the highest χ^2 deviation of 0.0017, whereas the model curves fitted the experimental counterparts very well with the highest χ^2

of 0.0103. The conformity of experimental EIS spectra with KKT standard confirmed the proposed EEC model (Fig. 8).

Fig. 9 depicts the evolution of R_{CT} , R_F , C_{DL} and C_F over time for all the investigated d_{elec} . C_{DL} values estimated correspond well to the average values widely reported in literature (4-60 μF) [36, 48, 50, 62, 93, 105, 106]. An interesting feature is that R_{CT} and C_{DL} values were seen to be constant over the course of experiment, whatever the d_{elec} adopted (Fig. 9). The average values of R_{CT} were $0.79 \pm 0.04 \Omega$, $0.55 \pm 0.05 \Omega$, $1.1 \pm 0.14 \Omega$, $1.6 \pm 0.06 \Omega$ and $4.4 \pm 0.18 \Omega$ for 100, 250, 500, 1000 and 3000 μm d_{elec} respectively. The average C_{DL} values were $25 \pm 1.7 \mu F$, $21 \pm 2.4 \mu F$, $8 \pm 1.3 \mu F$, $6.2 \pm 0.2 \mu F$ and $2.6 \pm 0.1 \mu F$ for respective distances of 100, 250, 500, 1000 and 3000 μm . In literature, R_{CT} and C_{DL} have been reported to respectively increase and decrease as function of electrolysis time [4, 6, 28, 36, 50, 93, 94], due to non-conductive nature of $CaCO_3$ and $Mg(OH)_2$ deposits which progressively cover the effective surface of electrode. Contrastingly, under this experimental setup, the progressive formation of mineral electro-precipitate did not significantly impede the electrochemical reactions occurring on the electrode/electrolyte interface. This observation could be attributed to the large cathode surface used in these experiments, which was about 25 to 250 times bigger than the classic rotating disk electrodes used by others [46]. The cathode surface was not fully covered by the precipitates hence offered adequate sites for electronic exchanges at electrode/electrolyte interface. Moreover, owing to concomitant gas evolution on the cathode, the morphology of electro-precipitate is known to be porous which hindered the complete coverage of cathode surface [48, 107]. Finally, the overall trend of the impedance response attributed to the faradaic resistance of non-conducting porous layer (R_F) was found to increase over time according to Fig. 9. The increase was more pronounced under the configuration in which more mineral electro-precipitation occurred, i.e., when d_{elec} was decreasing. After 5 h of electrolysis, there was an increase of about 1.1, 1.3, 2.1, 2.5 and 3.7 times of R_F relatively to their initial values before electrolysis for the respective distances of 3000, 1000, 500, 250 and 100 μm . In the

meantime, C_F appeared to be rather constant during the electrolysis considering standard deviations, similarly to the evolution of C_{DL} with electrolysis time (Fig. 9).

Fig. 10 illustrates the experimental and modeling plots of R_{CT} and C_{DL} as a function of d_{elec} at the beginning and after 1, 3 and 5 h of electrolysis. Interestingly, R_{CT} increased linearly with increasing d_{elec} according to Figs. 10a, 10c, 10e and 10g. At $t = 0$, the linear curve has a slope of $1.20 \Omega \text{ mm}^{-1}$ ($R^2 = 0.99$) and after 5 h electrolysis, the slope was evaluated at $1.43 \Omega \text{ mm}^{-1}$ ($R^2 = 0.98$). One could expect that the more the electrode is covered by non-conducting film, the more the R_{CT} resistance for faradaic electron exchange at electrode/electrolyte is enhanced. This reverse trend can be firstly explained by the manifestation of varying the d_{elec} . It has been elaborated from Fig. 4 that the involvement of anodic activity producing dissolved O_2 was more pronounced in microfluidic configuration. As a result, R_{CT} measured by EIS at narrow interelectrode gap was lower. Secondly, as depicted in Fig. 2, when d_{elec} increased, the E_C measured on cathode surface decreased lower into the water reduction region. More vigorous HER occurring at higher d_{elec} impeded more effectively the electronic charge transfer. As a result, R_{CT} increased as the interelectrode gap increased. Those are the reasons why largest R_{CT} was characterized with 3000 μm setup in Fig. 10 despite the least mineral scaling occurred under this configuration. Moreover, the fact that R_{CT} decreased when E_C increased (i.e., when d_{elec} decreased) does corroborate the result obtained by Hoseinie et al. [38]. Eventually, the trend of R_{CT} as function of d_{elec} offers a new interesting insight, since it has never been studied elsewhere in the literature and therefore constitutes a baseline for future investigation.

To further explore the trend between R_{CT} and the d_{elec} , the slopes of R_{CT} curves (R_{CT}/d_{elec}) obtained in Figs. 10a, 10c, 10e and 10g have been plotted as function of electrolysis time (Fig. 11). It was noticed that the R_{CT}/d_{elec} ratio remained practically constant and it took an average value of $1.32 \pm 0.11 \Omega \text{ mm}^{-1}$ during the electrolysis. This finding suggested that the electrochemical setup adopted in this work was not prone to prompt total electrode passivation by mineral scaling, at least

after 5 h of electrolysis. This is probably due to the large effective surface area employed in this work and further highlights its interest for the application at larger scale.

Looking at the redistribution of charges at the electrode/electrolyte interface (**Fig. 10b, 10d, 10f and 10h**), another new interesting insight was noticed. C_{DL} values decreased drastically with increasing d_{elec} . This could partly be attributed to the decrease in the applied E_C on cathode. As the consequence of more vigorous gas evolution at lower E_C , the distribution of charges at cathode/electrolyte interface was perturbed and ionic species and their solvated forms could undergo rearrangement at the interface [108-110]. As a result, the capacitance response via EIS measurement was smaller. The apparent decreasing trend of C_{DL} values with decreasing E_C was supported by the literature [48, 91, 92, 96, 111]. Furthermore, a new model is proposed to establish the relationship between C_{DL} and d_{elec} . C_{DL} model curves are plotted as a function of d_{elec} in **Fig. 10b, 10d, 10f and 10h** before ($t = 0$) and after 1, 3 and 5 h of electrolysis using **Eq. (29)**.

$$C_{DL} = 5.0305 \pm 0.6073 \times \frac{1}{d_{elec}} \quad (29)$$

In **Eq. (29)**, C_{DL} is expressed in μF and d_{elec} is in mm. It can be observed that C_{DL} varied linearly with $1/d_{elec}$ from millimetric distances down to 250 μm . Within this range of d_{elec} , the theoretical C_{DL} curves matched well the experimental plots. Using ME fitting criterion (**Eq. (21)**), the ME was evaluated as high as 97.93% with the worst fitting scenario calculated to be 95.46%. Below 250 μm , the evolution of C_{DL} was no longer proportional to the inverse of d_{elec} . More mineral scaling occurring under this condition might be the factor that broke the linearity with $1/d_{elec}$.

By identification between **Eq. (29)** and **Eq. (19)**, the slope of the former equals to $2\varepsilon_S\varepsilon_0k$. Thus, the constant k can be estimated and equaled to 3.55×10^6 . Computing **Eq. (18)** with the approximated k yielded d_{DL} values of 0.07, 0.14, 0.28 and 0.85 nm when the electrochemical cell was equipped with 250, 500, 1000 and 3000 μm d_{elec} respectively. These values were lower than 3 to 5 nm reported in diluted aqueous solution (10 mM of electrolyte) at 25°C [59, 112]. This difference might

be explained by the concurrent gas evolution taking place in the present case on both cathode and anode surfaces through the entire electrolysis.

On the contrary, the evolutions of R_F and C_F which are characteristic of insulating deposit films formed on cathode surface as function of d_{elec} (**Fig. S5**) were more straightforward. Both resistance and capacitance related to the film formation (i.e., R_F and C_F , respectively) decreased in the increasing order of d_{elec} . As depicted in **Fig. 1**, less mineral deposition took place in the increasing order of interelectrode gap. Consequently, fitted R_F and C_F values decreased owing to lesser mineral electro-precipitation formed in ascending order of d_{elec} . This further emphasizes the decreasing trends of R_F and C_F values with decreasing applied potential which have been reported in literature **[36, 48, 91, 93, 96]**.

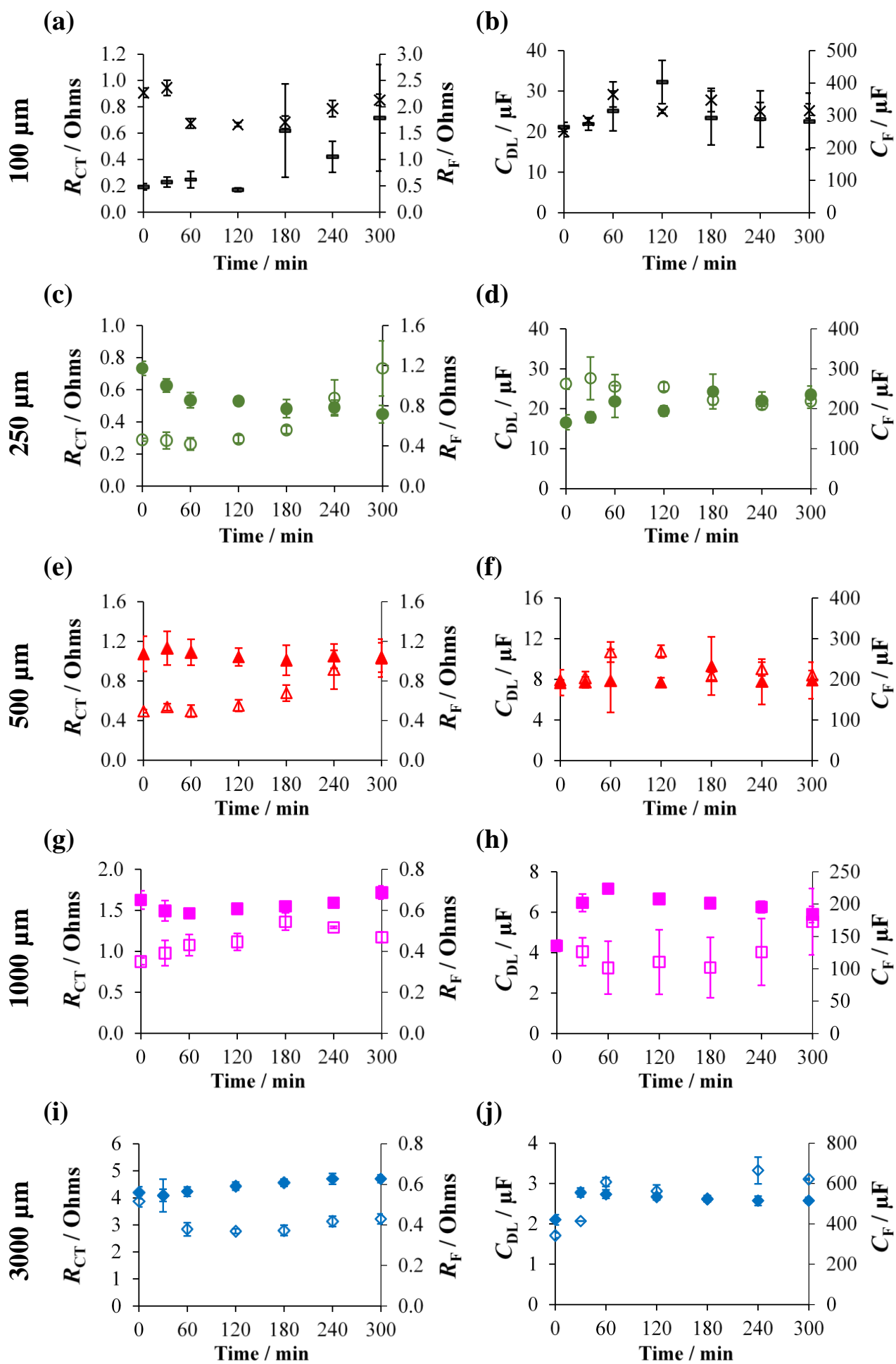


Fig. 9. Evolution of R_{CT} (✕, ●, ▲, ■, ◆), R_F (—, ○, △, □, ◇) in (a), (c), (e), (g), (i) as well as C_{DL} (✕, ●, ▲, ■, ◆) and C_F (—, ○, △, □, ◇) in (b), (d), (f), (h), (j) during 5 h of electrolysis using different d_{elec} . Cathode: SS, anode: BDD and j_{app} : 4 mA cm⁻². Solution containing 150 mg L⁻¹ of Ca²⁺, 5 mg L⁻¹ of Mg²⁺ and 60 mg L⁻¹ of TIC.

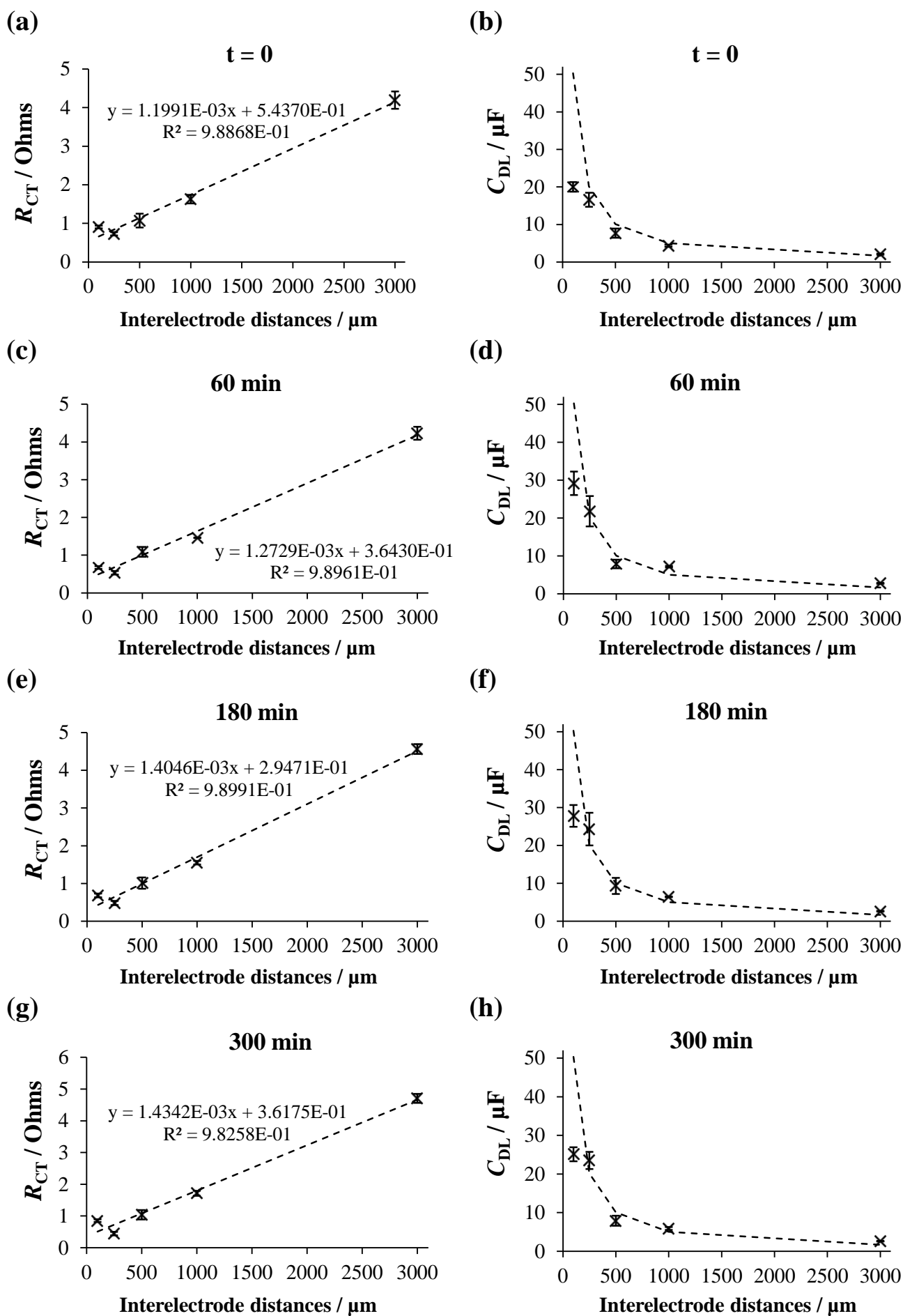


Fig. 10. Experimental and modeled curves of R_{CT} in (a), (c), (e) and (g) as well as C_{DL} in (b), (d), (f) and (h) as function of d_{elec} at the initial time and after 1, 3 and 5 h of electrolysis. Cathode: SS, anode: BDD and j_{app} : 4 mA cm^{-2} . Solution containing 150 mg L^{-1} of Ca^{2+} , 5 mg L^{-1} of Mg^{2+} and 60 mg L^{-1} of TIC.

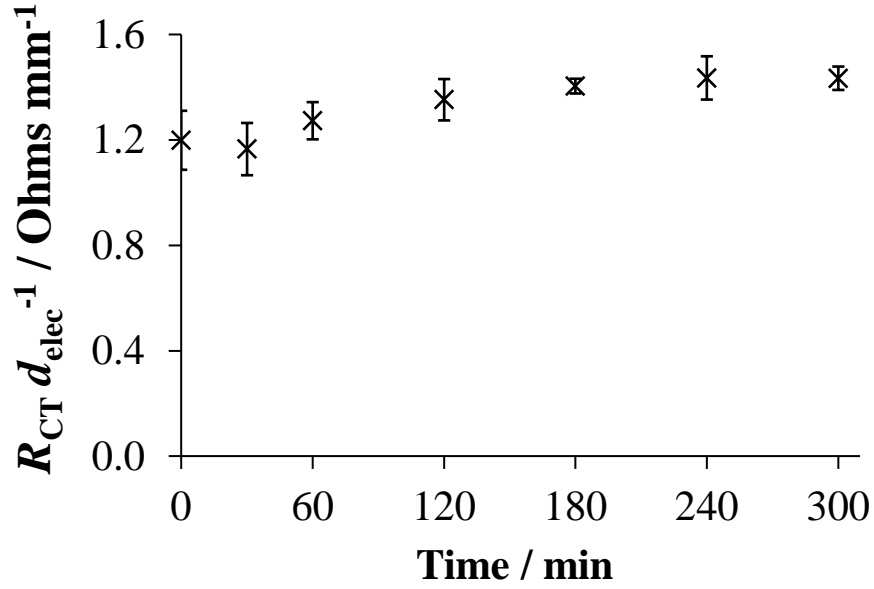


Fig. 11. R_{CT}/d_{elec} slope as a function of electrolysis time.

5. Conclusions

The influence of a wide range of d_{elec} (50-3000 μm) towards the occurrence of mineral electro-precipitation has been elucidated for the first time. Under similar diffusional mass transport regime and laminar hydrodynamic regime from one configuration to the others, more deposition of $\text{Mg}(\text{OH})_2$ and CaCO_3 were observed in decreasing order of d_{elec} from 3000 to 100 μm , whilst no deposit was present at the lowest d_{elec} investigated (50 μm). This new insight was mostly accounted for the applied E_C when the electrochemical cells were polarized at 4 mA cm^{-2} . No OH^- was yet produced under the 50 μm configuration, due to the high E_C value ($0.202 \pm 0.024 \text{ V/Ag-AgCl}$). From 100 μm d_{elec} upwards, the OH^- production occurred concomitantly with HER and it was more intense at higher interelectrode gap. This finding was in line with the decreasing measured E_C in ascending order of d_{elec} . In this case, the concurrent HER on one hand, hindered the transport of Mg^{2+} , Ca^{2+} and carbonates towards cathode surface and on the other induced detachment of mineral scaling. When identical E_C was applied under millimetric and microfluidic configurations, a difference of electro-precipitation related to the electrochemical reactor design was emphasized. More provision of dissolved O_2 produced from OER on anode contributed towards the formation of mineral scaling on cathode under microfluidic than millimetric setup.

A novel mathematical modeling taking into account the concomitant H_2 evolution to model the kinetics of Mg and Ca electro-precipitation has been proposed. It fitted well with the experimental data (RMSE < 0.0109 for Mg^{2+} and RMSE < 0.1435 for Ca^{2+}). The concurrent gas bubbles formed while varying d_{elec} showed that both relative resistivity and gas void fraction increased when d_{elec} decreased from 3000 μm to 100 μm . Despite the concomitant HER, when d_{elec} was reduced, the internal ohmic resistance dropped linearly with decreasing interelectrode gap from millimetric down to 100 μm , but below 100 μm , the linear trend was no longer observed.

Electrochemical processes taking place at the cathode/electrolyte interface was accessed by EIS method. Under the configurations where mineral deposition were observed, it was noticed that the

R_{CT} and C_{DL} values were constant during the 5 h of electrolysis whatever the d_{elec} adopted. It was attributed to the large effective surface area of the cathode whereby it was not fully passivated under the applied operating conditions in this work. Contrastingly, R_{CT} and C_{DL} values increased and decreased respectively with increasing d_{elec} . Under microfluidic setups, R_{CT} values were lower owing firstly to the facility of OH^- production due to external provision of dissolved O_2 from the oxidation of water on anode, and secondly to the less evolving H_2 at lower d_{elec} . Using higher d_{elec} , higher intensity of HER provoked more perturbation of charge distribution at electrode/electrolyte interface, which resulted in lower C_{DL} values. Novel mathematical relations to relate R_{CT} and C_{DL} with d_{elec} have been proposed to predict their evolution.

Finally, it has been newly demonstrated the importance of d_{elec} on the formation of mineral scaling on cathode surface. Both the effects of H_2 overpotential and electrochemical design (i.e., the contribution of anode under micrometric distances) have been proven influential to hinder or minimize the occurrence of mineral precipitation on cathode surface through the occurrence or not of gas bubbles electrogeneration. Due to primordial role of gas evolution taking an effect on mineral electro-precipitation observed in this work, the overpotential of H_2 evolution offered by other cathode materials could either minimize or maximize the electro-precipitation, which will be the subject of research in incoming works.

Acknowledgments

Authors would like to express sincere gratitude to French Ministry of Higher Education and Research (MESRI) for financial grant of doctorate program for Faizul Hakim Adnan as well as other fundings provided by Carnot ICEEL, LTSER Zone Atelier du Bassin de la Moselle (ZAM) and European regional development fund program (CPER SusChemProc).

Appendix A. Supplementary data

Supplementary data associated with this article can be found, in the online version, at ***.

References

- [1] C. Deslouis, I. Frateur, G. Maurin, B. Tribollet, Interfacial pH measurement during the reduction of dissolved oxygen in a submerged impinging jet cell, *Journal of Applied Electrochemistry* 27(4) (1997) 482-492. <https://doi.org/10.1023/A:1018430224622>.
- [2] H. Deligianni, L.T. Romankiw, In situ surface pH measurement during electrolysis using a rotating pH electrode, *IBM Journal of Research and Development* 37(2) (1993) 85-95. <https://doi.org/10.1147/rd.372.0085>.
- [3] Y. Lei, B. Song, R.D. van der Weijden, M. Saakes, C.J.N. Buisman, Electrochemical induced calcium phosphate precipitation: Importance of local pH, *Environmental Science & Technology* 51(19) (2017) 11156-11164. <https://doi.org/10.1021/acs.est.7b03909>.
- [4] C. Deslouis, D. Festy, O. Gil, V. Maillot, S. Touzain, B. Tribollet, Characterization of calcareous deposits in artificial sea water by impedances techniques: 2-deposit of $\text{Mg}(\text{OH})_2$ without CaCO_3 , *Electrochimica Acta* 45(11) (2000) 1837-1845.
- [5] L. Beaunier, C. Gabrielli, G. Poindessous, G. Maurin, R. Rosset, Investigation of electrochemical calcareous scaling: Nuclei counting and morphology, *Journal of Electroanalytical Chemistry* 501(1-2) (2001) 41-53.
- [6] C. Deslouis, D. Festy, O. Gil, G. Rius, S. Touzain, B. Tribollet, Characterization of calcareous deposits in artificial sea water by impedance techniques — 1. Deposit of CaCO_3 without $\text{Mg}(\text{OH})_2$, *Electrochimica Acta* 43(12-13) (1998) 1891-1901.
- [7] O. Garcia-Rodriguez, E. Mousset, H. Olvera-Vargas, O. Lefebvre, Electrochemical treatment of highly concentrated wastewater: A review of experimental and modeling approaches from lab- to full-scale, *Critical Reviews in Environmental Science and Technology* (2020) 1-70. <https://doi.org/10.1080/10643389.2020.1820428>.
- [8] C.A. Martínez-Huitle, M.A. Rodrigo, I. Sirés, O. Scialdone, Single and coupled electrochemical processes and reactors for the abatement of organic water pollutants: A critical review, *Chemical Reviews* 115(24) (2015) 13362-13407. <https://doi.org/10.1021/acs.chemrev.5b00361>.
- [9] F.C. Moreira, R.A.R. Boaventura, E. Brillas, V.J.P. Vilar, Electrochemical advanced oxidation processes: A review on their application to synthetic and real wastewaters, *Applied Catalysis B: Environmental* 202 (2017) 217-261. <https://doi.org/https://doi.org/10.1016/j.apcatb.2016.08.037>.
- [10] E. Mousset, D.D. Dionysiou, Photoelectrochemical reactors for treatment of water and wastewater: A review, *Environmental Chemistry Letters* 18(4) (2020) 1301-1318. <https://doi.org/10.1007/s10311-020-01014-9>.
- [11] E. Mousset, W.H. Loh, W.S. Lim, L. Jarry, Z. Wang, O. Lefebvre, Cost comparison of advanced oxidation processes for wastewater treatment using accumulated oxygen-equivalent criteria, *Water Research* 200 (2021) 117234. <https://doi.org/https://doi.org/10.1016/j.watres.2021.117234>.
- [12] O. Scialdone, A. Galia, C. Guarisco, S. Randazzo, G. Filardo, Electrochemical incineration of oxalic acid at boron doped diamond anodes: Role of operative parameters, *Electrochimica Acta* 53(5) (2008) 2095-2108. <https://doi.org/https://doi.org/10.1016/j.electacta.2007.09.007>.
- [13] O. Scialdone, E. Corrado, A. Galia, I. Sirés, Electrochemical processes in macro and microfluidic cells for the abatement of chloroacetic acid from water, *Electrochimica Acta* 132 (2014) 15-24. <https://doi.org/https://doi.org/10.1016/j.electacta.2014.03.127>.

- [14] O. Scialdone, A. Galia, S. Sabatino, D. Mira, C. Amatore, Electrochemical conversion of dichloroacetic acid to chloroacetic acid in a microfluidic stack and in a series of microfluidic reactors, *ChemElectroChem* 2(5) (2015) 684-690. <https://doi.org/doi:10.1002/celc.201402454>.
- [15] E. Mousset, Unprecedented reactive electro-mixing reactor: Towards synergy between micro- and macro-reactors?, *Electrochemistry Communications* 118 (2020) 106787. <https://doi.org/https://doi.org/10.1016/j.elecom.2020.106787>.
- [16] P.V. Nidheesh, G. Divyapriya, N. Oturan, C. Trellu, M.A. Oturan, Environmental applications of boron-doped diamond electrodes: 1. Applications in water and wastewater treatment, *ChemElectroChem* 6(8) (2019) 2124-2142. <https://doi.org/https://doi.org/10.1002/celc.201801876>.
- [17] S.O. Ganiyu, C.A. Martínez-Huitle, Nature, mechanisms and reactivity of electrogenerated reactive species at thin-film boron-doped diamond (BDD) electrodes during electrochemical wastewater treatment, *ChemElectroChem* 6(9) (2019) 2379-2392. <https://doi.org/https://doi.org/10.1002/celc.201900159>.
- [18] E. Mousset, N. Oturan, M.A. Oturan, An unprecedented route of OH radical reactivity evidenced by an electrocatalytic process: Ipso-substitution with perhalogenocarbon compounds, *Applied Catalysis B: Environmental* 226 (2018) 135-146. <https://doi.org/https://doi.org/10.1016/j.apcatb.2017.12.028>.
- [19] X. Du, M.A. Oturan, M. Zhou, N. Belkessa, P. Su, J. Cai, C. Trellu, E. Mousset, Nanostructured electrodes for electrocatalytic advanced oxidation processes: From materials preparation to mechanisms understanding and wastewater treatment applications, *Applied Catalysis B: Environmental* 296 (2021) 120332. <https://doi.org/https://doi.org/10.1016/j.apcatb.2021.120332>.
- [20] P. Ma, H. Ma, S. Sabatino, A. Galia, O. Scialdone, Electrochemical treatment of real wastewater. Part 1: Effluents with low conductivity, *Chemical Engineering Journal* 336 (2018) 133-140. <https://doi.org/https://doi.org/10.1016/j.cej.2017.11.046>.
- [21] E. Mousset, M. Puce, M.N. Pons, Advanced electro-oxidation with boron-doped diamond for acetaminophen removal from real wastewater in a microfluidic reactor: Kinetics and mass-transfer studies, *ChemElectroChem* 6(11) (2019) 2908-2916.
- [22] E. Mousset, L. Quackenbush, C. Schondek, A. Gerardin-Vergne, S. Pontvianne, S. Kmiotek, M.-N. Pons, Effect of homogeneous Fenton combined with electron transfer on the fate of inorganic chlorinated species in synthetic and reclaimed municipal wastewater, *Electrochimica Acta* 334 (2020) 135608. <https://doi.org/https://doi.org/10.1016/j.electacta.2019.135608>.
- [23] E. Mousset, S. Pontvianne, M.-N. Pons, Fate of inorganic nitrogen species under homogeneous Fenton combined with electro-oxidation/reduction treatments in synthetic solutions and reclaimed municipal wastewater, *Chemosphere* 201 (2018) 6-12. <https://doi.org/https://doi.org/10.1016/j.chemosphere.2018.02.142>.
- [24] J. Marin-Cruz, R. Cabrera-Sierra, M. Pech-Canul, I. Gonzalez, EIS study on corrosion and scale processes and their inhibition in cooling system media, *Electrochimica Acta* 51(8-9) (2006) 1847-1854.
- [25] J. Marin-Cruz, E. Garcia-Figueroa, M. Miranda-Hernández, I. Gonzalez, Electrochemical treatments for selective growth of different calcium carbonate allotropic forms on carbon steel, *Water Research* 38(1) (2004) 173-183.
- [26] Y. Ben Amor, L. Bousselmi, H. Takenouti, E. Triki, Influence of sulphate ions on corrosion mechanism of carbon steel in calcareous media, *Corrosion Engineering, Science and Technology* 40(2) (2005) 129-136.
- [27] Y. Ben Amor, L. Bousselmi, B. Tribollet, E. Triki, Study of the effect of magnesium concentration on the deposit of allotropic forms of calcium carbonate and related carbon steel interface behavior, *Electrochimica Acta* 55(16) (2010) 4820-4826. <https://doi.org/https://doi.org/10.1016/j.electacta.2010.01.109>.
- [28] L. Bousselmi, C. Fiaud, B. Tribollet, E. Triki, Impedance spectroscopic study of a steel electrode in condition of scaling and corrosion: Interphase model, *Electrochimica Acta* 44(24) (1999) 4357-4363. [https://doi.org/https://doi.org/10.1016/S0013-4686\(99\)00151-6](https://doi.org/https://doi.org/10.1016/S0013-4686(99)00151-6).
- [29] L. Bousselmi, C. Fiaud, B. Tribollet, E. Triki, The characterisation of the coated layer at the interface carbon steel-natural salt water by impedance spectroscopy, *Corrosion Science* 39(9) (1997) 1711-1724. [https://doi.org/https://doi.org/10.1016/S0010-938X\(97\)00077-2](https://doi.org/https://doi.org/10.1016/S0010-938X(97)00077-2).
- [30] Z. Belarbi, B. Sotta, L. Makhlofi, B. Tribollet, J. Gamby, Modelling of delay effect of calcium carbonate deposition kinetics on rotating disk electrode in the presence of green inhibitor, *Electrochimica Acta* 189 (2016) 118-127. <https://doi.org/https://doi.org/10.1016/j.electacta.2015.12.089>.

- [31] M. Euvrad, F. Membrey, C. Filiatre, C. Pignolet, A. Foissy, Kinetic study of the electrocrystallization of calcium carbonate on metallic substrates, *Journal Of Crystal Growth* 291(2) (2006) 428-435. <https://doi.org/https://doi.org/10.1016/j.jcrysgr.2006.03.025>.
- [32] R. Jaouhari, A. Benbachir, A. Guenbour, C. Gabrielli, J. Garcia-Jareno, G. Maurin, Influence of water composition and substrate on electrochemical scaling, *Journal of The Electrochemical Society* 147(6) (2000) 2151-2161. <https://doi.org/10.1149/1.1393501>.
- [33] A. Martinod, A. Neville, M. Euvrad, K. Sorbie, Electrodeposition of a calcareous layer: Effects of green inhibitors, *Chemical Engineering Science* 64(10) (2009) 2413-2421. <https://doi.org/https://doi.org/10.1016/j.ces.2009.01.024>.
- [34] C. Deslouis, P. Falaras, O. Gil, M. Jeannin, V. Maillot, B. Tribollet, Influence of clay on calcareous deposit in natural and artificial sea water, *Electrochimica Acta* 51(15) (2006) 3173-3180. <https://doi.org/https://doi.org/10.1016/j.electacta.2005.09.006>.
- [35] S.-H. Lin, S.C. Dexter, Effects of temperature and magnesium ions on calcareous deposition, *Corrosion* 44(9) (1988) 615-622. <https://doi.org/10.5006/1.3584974>.
- [36] J. Marin-Cruz, R. Cabrera-Sierra, M. Pech-Canul, I. Gonzalez, Characterization of different allotropic forms of calcium carbonate scales on carbon steel by electrochemical impedance spectroscopy, *Journal of Applied Electrochemistry* 34(3) (2004) 337-343.
- [37] S.M. Hoseinie, T. Shahrabi, Influence of ionic species on scaling and corrosion performance of AISI 316L rotating disk electrodes in artificial seawater, *Desalination* 409 (2017) 32-46. <https://doi.org/https://doi.org/10.1016/j.desal.2017.01.017>.
- [38] S.M. Hoseinie, T. Shahrabi, B. Ramezanzadeh, M.F. Rad, The role of porosity and surface morphology of calcium carbonate deposits on the corrosion behavior of unprotected API 5L X52 rotating disk electrodes in artificial seawater, *Journal of The Electrochemical Society* 163(9) (2016) C515-C529. <https://doi.org/10.1149/2.0191609jes>.
- [39] B.S. Lalia, A. Khalil, R. Hashaiekh, Selective electrochemical separation and recovery of calcium and magnesium from brine, *Separation and Purification Technology* 264 (2021) 118416. <https://doi.org/https://doi.org/10.1016/j.seppur.2021.118416>.
- [40] B.S. Lalia, R. Hashaiekh, Electrochemical precipitation to reduce waste brine salinity, *Desalination* 498 (2021) 114796. <https://doi.org/https://doi.org/10.1016/j.desal.2020.114796>.
- [41] Y. Lei, J.C. Remmers, M. Saakes, R.D. van der Weijden, C.J.N. Buisman, Is there a precipitation sequence in municipal wastewater induced by electrolysis?, *Environmental Science & Technology* 52(15) (2018) 8399-8407. <https://doi.org/10.1021/acs.est.8b02869>.
- [42] Y. Lei, B. Song, M. Saakes, R.D. van der Weijden, C.J.N. Buisman, Interaction of calcium, phosphorus and natural organic matter in electrochemical recovery of phosphate, *Water Research* 142 (2018) 10-17. <https://doi.org/https://doi.org/10.1016/j.watres.2018.05.035>.
- [43] Y. Lei, I. Hidayat, M. Saakes, R. van der Weijden, C.J.N. Buisman, Fate of calcium, magnesium and inorganic carbon in electrochemical phosphorus recovery from domestic wastewater, *Chemical Engineering Journal* 362 (2019) 453-459. <https://doi.org/https://doi.org/10.1016/j.cej.2019.01.056>.
- [44] Y. Lei, E. Geraets, M. Saakes, R.D. van der Weijden, C.J.N. Buisman, Electrochemical removal of phosphate in the presence of calcium at low current density: Precipitation or adsorption ?, *Water Research* 169 (2020) 115207. <https://doi.org/https://doi.org/10.1016/j.watres.2019.115207>.
- [45] I. Sanjuán, D. Benavente, V. García-García, E. Expósito, V. Montiel, Electrochemical softening of concentrates from an electrodialysis brackish water desalination plant: Efficiency enhancement using a three-dimensional cathode, *Separation and Purification Technology* 208 (2019) 217-226. <https://doi.org/https://doi.org/10.1016/j.seppur.2018.01.066>.
- [46] F.H. Adnan, E. Mousset, S. Pontvianne, M.-N. Pons, Mineral cathodic electro-precipitation and its kinetic modelling in thin-film microfluidic reactor during advanced electro-oxidation process, *Electrochimica Acta* (2021) 138487. <https://doi.org/https://doi.org/10.1016/j.electacta.2021.138487>.
- [47] C. Barchiche, C. Deslouis, D. Festy, O. Gil, P. Refait, S. Touzain, B. Tribollet, Characterization of calcareous deposits in artificial seawater by impedance techniques: 3 — deposit of CaCO₃ in the presence of Mg(II), *Electrochimica Acta* 48(12) (2003) 1645-1654.

- [48] M. Piri, R. Arefinia, Investigation of the hydrogen evolution phenomenon on CaCO_3 precipitation in artificial seawater, *Desalination* 444 (2018) 142-150. <https://doi.org/https://doi.org/10.1016/j.desal.2018.05.018>.
- [49] H. Karoui, B. Riffault, M. Jeannin, A. Kahoul, O. Gil, M. Ben Amor, M.M. Tlili, Electrochemical scaling of stainless steel in artificial seawater: Role of experimental conditions on CaCO_3 and $\text{Mg}(\text{OH})_2$ formation, *Desalination* 311 (2013) 234-240. <https://doi.org/https://doi.org/10.1016/j.desal.2012.07.011>.
- [50] C. Gabrielli, M. Keddam, A. Khalil, R. Rosset, M. Zidoune, Study of calcium carbonate scales by electrochemical impedance spectroscopy, *Electrochimica Acta* 42(8) (1997) 1207-1218.
- [51] F.H. Adnan, M.-N. Pons, E. Mousset, Mass transport evolution in microfluidic thin film electrochemical reactors: New correlations from millimetric to submillimetric interelectrode distances, *Electrochemistry Communications* 130 (2021) 107097. <https://doi.org/https://doi.org/10.1016/j.elecom.2021.107097>.
- [52] W. Khongthong, G. Jovanovic, A. Yokochi, P. Sangvanich, V. Pavarajarn, Degradation of diuron via an electrochemical advanced oxidation process in a microscale-based reactor, *Chemical Engineering Journal* 292 (2016) 298-307. <https://doi.org/https://doi.org/10.1016/j.cej.2016.02.042>.
- [53] J.C. Eklund, A.M. Bond, J.A. Alden, R.G. Compton, Perspectives in modern voltammetry: Basic concepts and mechanistic analysis, in: D. Bethell (Ed.), *Advances in Physical Organic Chemistry*, Academic Press 1999, pp. 1-120. [https://doi.org/https://doi.org/10.1016/S0065-3160\(08\)60006-4](https://doi.org/https://doi.org/10.1016/S0065-3160(08)60006-4).
- [54] D.J. Pickett, B.R. Stanmore, Ionic mass transfer in parallel plate electrochemical cells, *Journal of Applied Electrochemistry* 2(2) (1972) 151-156. <https://doi.org/10.1007/BF00609131>.
- [55] F. Cœuret, A. Storck, *Hydrodynamique et transfert de matière par diffusion*, *Éléments de génie électrochimique*, Lavoisier, Paris, 1993, pp. 91-128.
- [56] J.N. Butler, *Carbon dioxide equilibria and their applications*, 1st ed., Taylor & Francis Group, New York: Routledge, 1991. <https://doi.org/https://doi.org/10.1201/9781315138770>.
- [57] N. Xu, J. Riley, Nonlinear analysis of a classical system: The double-layer capacitor, *Electrochemistry Communications* 13(10) (2011) 1077-1081. <https://doi.org/https://doi.org/10.1016/j.elecom.2011.07.003>.
- [58] A.J. Bard, Faulkner, L.R., Double-layer structure and adsorption, in: J.W.S. Inc. (Ed.), *Electrochemical methods: Fundamentals and applications* 2001, p. 534.
- [59] B.E. Conway, J.O.M. Bockris, I.A. Ammar, The dielectric constant of the solution in the diffuse and Helmholtz double layers at a charged interface in aqueous solution, *Transactions of the Faraday Society* 47(0) (1951) 756-766. <https://doi.org/10.1039/TF9514700756>.
- [60] O. Teschke, G. Ceotto, E.F. de Souza, Interfacial water dielectric-permittivity-profile measurements using atomic force microscopy, *Physical Review E* 64(1) (2001) 011605. <https://doi.org/10.1103/PhysRevE.64.011605>.
- [61] M.C.F. Wander, A.E. Clark, Structural and dielectric properties of quartz–water interfaces, *The Journal of Physical Chemistry C* 112(50) (2008) 19986-19994. <https://doi.org/10.1021/jp803642c>.
- [62] M.E. Orazem, Tribollet, B., *Electrochemistry*, in: E.-E. Society (Ed.), *Electrochemical Impedance Spectroscopy* 2017, pp. 122-124. <https://doi.org/https://doi.org/10.1002/9781119363682.ch5>.
- [63] P. Reichert, AQUASIM - a tool for simulation and data analysis of aquatic systems, *Water Science and Technology* 30(2) (1994) 21.
- [64] E. Mousset, L. Frunzo, G. Esposito, E.D.v. Hullebusch, N. Oturan, M.A. Oturan, A complete phenol oxidation pathway obtained during electro-Fenton treatment and validated by a kinetic model study, *Applied Catalysis B: Environmental* 180 (2016) 189-198. <https://doi.org/https://doi.org/10.1016/j.apcatb.2015.06.014>.
- [65] M.M. Tlili, M. Benamor, C. Gabrielli, H. Perrot, B. Tribollet, Influence of the interfacial pH on electrochemical CaCO_3 precipitation, *Journal of The Electrochemical Society* 150(11) (2003) C765. <https://doi.org/10.1149/1.1613294>.
- [66] C. Carré, A. Zanibellato, M. Jeannin, R. Sabot, P. Gunkel-Grillon, A. Serres, Electrochemical calcareous deposition in seawater. A review, *Environmental Chemistry Letters* 18(4) (2020) 1193-1208. <https://doi.org/10.1007/s10311-020-01002-z>.
- [67] C. Arkam, Quartz crystal electrogravimetry with controlled hydrodynamics, *Journal of The Electrochemical Society* 141(9) (1994) L103. <https://doi.org/10.1149/1.2055167>.

- [68] H. Vogt, R.J. Balzer, The bubble coverage of gas-evolving electrodes in stagnant electrolytes, *Electrochimica Acta* 50(10) (2005) 2073-2079. <https://doi.org/https://doi.org/10.1016/j.electacta.2004.09.025>.
- [69] X. Hu, X. Tian, Y.-W. Lin, Z. Wang, Nickel foam and stainless steel mesh as electrocatalysts for hydrogen evolution reaction, oxygen evolution reaction and overall water splitting in alkaline media, *RSC Advances* 9(54) (2019) 31563-31571. <https://doi.org/10.1039/C9RA07258F>.
- [70] M. Wang, W. Fu, L. Du, Y. Wei, P. Rao, L. Wei, X. Zhao, Y. Wang, S. Sun, Surface engineering by doping manganese into cobalt phosphide towards highly efficient bifunctional HER and OER electrocatalysis, *Applied Surface Science* 515 (2020) 146059. <https://doi.org/https://doi.org/10.1016/j.apsusc.2020.146059>.
- [71] E. Mousset, Y. Pechaud, N. Oturan, M.A. Oturan, Charge transfer/mass transport competition in advanced hybrid electrocatalytic wastewater treatment: Development of a new current efficiency relation, *Applied Catalysis B: Environmental* 240 (2019) 102-111. <https://doi.org/https://doi.org/10.1016/j.apcatb.2018.08.055>.
- [72] O. Scialdone, C. Guarisco, A. Galia, Oxidation of organics in water in microfluidic electrochemical reactors: Theoretical model and experiments, *Electrochimica Acta* 58 (2011) 463-473. <https://doi.org/https://doi.org/10.1016/j.electacta.2011.09.073>.
- [73] S. Mathé, *Chimie des solutions*, Dunod 2018.
- [74] W.M. Haynes, *CRC Handbook of chemistry and physics*, 97th ed., CRC press 2017.
- [75] O. Velts, M. Uibu, J. Kallas, R. Kuusik, CO₂ mineral trapping: Modeling of calcium carbonate precipitation in a semi-batch reactor, *Energy Procedia* 4 (2011) 771-778.
- [76] S.J. Kakaraniya, A. Mehra, Reactive precipitation in gas-liquid systems, *Industrial & Engineering Chemistry Research* 46(4) (2007) 1125-1137. <https://doi.org/10.1021/ie0605128>.
- [77] C. Kazadi Mbamba, D.J. Batstone, X. Flores-Alsina, S. Tait, A generalised chemical precipitation modelling approach in wastewater treatment applied to calcite, *Water Research* 68 (2015) 342-353. <https://doi.org/https://doi.org/10.1016/j.watres.2014.10.011>.
- [78] O. Devos, C. Gabrielli, B. Tribollet, Nucleation-growth process of scale electrodeposition—Influence of the mass transport, *Electrochimica Acta* 52(1) (2006) 285-291. <https://doi.org/https://doi.org/10.1016/j.electacta.2006.05.008>.
- [79] D.A. Armstrong, R.E. Huie, W.H. Koppenol, S.V. Lyman, G. Merényi, P. Neta, B. Ruscic, D.M. Stanbury, S. Steenken, P. Wardman, Standard electrode potentials involving radicals in aqueous solution: inorganic radicals (IUPAC Technical Report), *Pure and Applied Chemistry* 87(11-12) (2015) 1139-1150. <https://doi.org/doi:10.1515/pac-2014-0502>.
- [80] P. Mandin, Z. Derhoumi, H. Roustan, W. Rolf, Bubble over-potential during two-phase alkaline water electrolysis, *Electrochimica Acta* 128 (2014) 248-258. <https://doi.org/https://doi.org/10.1016/j.electacta.2013.11.068>.
- [81] R. Hreiz, L. Abdelouahed, D. Fünfschilling, F. Lapique, Electrogenated bubbles induced convection in narrow vertical cells: A review, *Chemical Engineering Research and Design* 100 (2015) 268-281. <https://doi.org/https://doi.org/10.1016/j.cherd.2015.05.035>.
- [82] R. Hreiz, L. Abdelouahed, D. Fünfschilling, F. Lapique, Electrogenated bubbles induced convection in narrow vertical cells: PIV measurements and Euler–Lagrange CFD simulation, *Chemical Engineering Science* 134 (2015) 138-152. <https://doi.org/https://doi.org/10.1016/j.ces.2015.04.041>.
- [83] L. Abdelouahed, G. Valentin, S. Poncin, F. Lapique, Current density distribution and gas volume fraction in the gap of lantern blade electrodes, *Chemical Engineering Research and Design* 92(3) (2014) 559-570. <https://doi.org/https://doi.org/10.1016/j.cherd.2013.10.003>.
- [84] F. Hine, Bubble effects on the solution ir drop in a vertical electrolyzer under free and forced convection, *Journal of The Electrochemical Society* 127(2) (1980) 292. <https://doi.org/10.1149/1.2129658>.
- [85] F. Hine, Hydrodynamic studies of bubble effects on the IR-drops in a vertical rectangular cell, *Journal of The Electrochemical Society* 122(9) (1975) 1185. <https://doi.org/10.1149/1.2134422>.
- [86] H. Vogt, A hydrodynamic model for the ohmic interelectrode resistance of cells with vertical gas evolving electrodes, *Electrochimica Acta* 26(9) (1981) 1311-1317. [https://doi.org/https://doi.org/10.1016/0013-4686\(81\)85115-8](https://doi.org/https://doi.org/10.1016/0013-4686(81)85115-8).

- [87] X. Chen, G. Chen, P.L. Yue, Investigation on the electrolysis voltage of electrocoagulation, *Chemical Engineering Science* 57(13) (2002) 2449-2455. [https://doi.org/https://doi.org/10.1016/S0009-2509\(02\)00147-1](https://doi.org/https://doi.org/10.1016/S0009-2509(02)00147-1).
- [88] G.J. Brug, A.L.G. van den Eeden, M. Sluyters-Rehbach, J.H. Sluyters, The analysis of electrode impedances complicated by the presence of a constant phase element, *Journal of Electroanalytical Chemistry and Interfacial Electrochemistry* 176(1) (1984) 275-295. [https://doi.org/https://doi.org/10.1016/S0022-0728\(84\)80324-1](https://doi.org/https://doi.org/10.1016/S0022-0728(84)80324-1).
- [89] B. Hirschorn, M.E. Orazem, B. Tribollet, V. Vivier, I. Frateur, M. Musiani, Determination of effective capacitance and film thickness from constant-phase-element parameters, *Electrochimica Acta* 55(21) (2010) 6218-6227. <https://doi.org/https://doi.org/10.1016/j.electacta.2009.10.065>.
- [90] M.E. Orazem, Tribollet, B., Time-constant dispersion, in: E.-E. Society (Ed.), *Electrochemical Impedance Spectroscopy*, John Wiley & Sons, Inc2017, pp. 349-355. <https://doi.org/https://doi.org/10.1002/9781119363682.ch13>.
- [91] X. Cao, C. Jin, F. Lu, Z. Yang, M. Shen, R. Yang, Electrochemical properties of MnCo₂O₄ spinel bifunctional catalyst for oxygen reduction and evolution reaction, *Journal of The Electrochemical Society* 161(5) (2014) H296-H300. <https://doi.org/10.1149/2.029405jes>.
- [92] Y. Lai, Y. Li, L. Jiang, W. Xu, X. Lv, J. Li, Y. Liu, Electrochemical behaviors of co-deposited Pb/Pb-MnO₂ composite anode in sulfuric acid solution – Tafel and EIS investigations, *Journal of Electroanalytical Chemistry* 671 (2012) 16-23. <https://doi.org/https://doi.org/10.1016/j.jelechem.2012.02.011>.
- [93] O. Devos, C. Gabrielli, B. Tribollet, Simultaneous EIS and in situ microscope observation on a partially blocked electrode application to scale electrodeposition, *Electrochimica Acta* 51(8-9) (2006) 1413-1422.
- [94] X.-M. Wang, J.-M. Hu, J.-Q. Zhang, C.-N. Cao, Characterization of surface fouling of Ti/IrO₂ electrodes in 4-chlorophenol aqueous solutions by electrochemical impedance spectroscopy, *Electrochimica Acta* 53(8) (2008) 3386-3394. <https://doi.org/https://doi.org/10.1016/j.electacta.2007.11.070>.
- [95] L.A. da Silva, V.A. Alves, M.A.P. da Silva, S. Trasatti, J.F.C. Boodts, Electrochemical impedance, SEM, EDX and voltammetric study of oxygen evolution on Ir + Ti + Pt ternary-oxide electrodes in alkaline solution, *Electrochimica Acta* 41(7) (1996) 1279-1285. [https://doi.org/https://doi.org/10.1016/0013-4686\(95\)00448-3](https://doi.org/https://doi.org/10.1016/0013-4686(95)00448-3).
- [96] L.A. da Silva, V.A. Alves, M.A.P. da Silva, S. Trasatti, J.F.C. Boodts, Oxygen evolution in acid solution on IrO₂ + TiO₂ ceramic films. A study by impedance, voltammetry and SEM, *Electrochimica Acta* 42(2) (1997) 271-281. [https://doi.org/https://doi.org/10.1016/0013-4686\(96\)00160-0](https://doi.org/https://doi.org/10.1016/0013-4686(96)00160-0).
- [97] J.-M. Hu, J.-Q. Zhang, C.-N. Cao, I.M. Hsing, Kinetics investigation of H₂/CO electrooxidation in PEFCs by the combined use of equivalent circuit fitting and mathematical modeling of the faradaic impedance, *Electrochimica Acta* 49(28) (2004) 5227-5234. <https://doi.org/https://doi.org/10.1016/j.electacta.2004.07.004>.
- [98] E. Rasten, G. Hagen, R. Tunold, Electrocatalysis in water electrolysis with solid polymer electrolyte, *Electrochimica Acta* 48(25) (2003) 3945-3952. <https://doi.org/https://doi.org/10.1016/j.electacta.2003.04.001>.
- [99] M. Urquidi-Macdonald, S. Real, D.D. Macdonald, Applications of Kramers–Kronig transforms in the analysis of electrochemical impedance data—III. Stability and linearity, *Electrochimica Acta* 35(10) (1990) 1559-1566. [https://doi.org/https://doi.org/10.1016/0013-4686\(90\)80010-L](https://doi.org/https://doi.org/10.1016/0013-4686(90)80010-L).
- [100] M.E. Orazem, Tribollet, B., The Kramers–Kronig relations, in: E.-E. Society (Ed.), *Electrochemical Impedance Spectroscopy*, John Wiley & Sons, Inc2017, pp. 595-614. <https://doi.org/https://doi.org/10.1002/9781119363682.ch22>.
- [101] M.C.H. McKubre, D.D. Macdonald, B. Sayers, J.R. Macdonald, Measuring techniques and data analysis, *Impedance Spectroscopy*2018, pp. 124-126. <https://doi.org/https://doi.org/10.1002/9781119381860.ch3>.
- [102] R. Pachimatla, M. Thomas, S.R. Oc, R. Srinivasan, Analysis of instabilities in electrochemical systems using nonlinear electrochemical impedance spectroscopy, *Journal of The Electrochemical Society* 166(8) (2019) H304-H312. <https://doi.org/10.1149/2.0571908jes>.
- [103] B.A. Boukamp, A linear Kronig-Kramers transform test for immittance data validation, *Journal of The Electrochemical Society* 142(6) (1995) 1885-1894. <https://doi.org/10.1149/1.2044210>.
- [104] B.A. Boukamp, Electrochemical impedance spectroscopy in solid state ionics: recent advances, *Solid State Ionics* 169(1) (2004) 65-73. <https://doi.org/https://doi.org/10.1016/j.ssi.2003.07.002>.

- [105] C. Cachet, R. Wiert, Zinc electrowinning in acidic sulfate electrolytes: Impedance analysis and modeling of the influence on Nickel impurities, *Journal of The Electrochemical Society* 141(1) (1994) 131-140. <https://doi.org/10.1149/1.2054672>.
- [106] Y. Ge, X. Xie, J. Roscher, R. Holze, Q. Qu, How to measure and report the capacity of electrochemical double layers, supercapacitors, and their electrode materials, *Journal of Solid State Electrochemistry* 24(11) (2020) 3215-3230. <https://doi.org/10.1007/s10008-020-04804-x>.
- [107] C. Gabrielli, Quartz crystal microbalance investigation of electrochemical calcium carbonate scaling, *Journal of The Electrochemical Society* 145(7) (1998) 2386. <https://doi.org/10.1149/1.1838648>.
- [108] R.W. Impey, P.A. Madden, I.R. McDonald, Hydration and mobility of ions in solution, *The Journal of Physical Chemistry* 87(25) (1983) 5071-5083. <https://doi.org/10.1021/j150643a008>.
- [109] C. Zhong, Y. Deng, W. Hu, J. Qiao, L. Zhang, J. Zhang, A review of electrolyte materials and compositions for electrochemical supercapacitors, *Chemical Society Reviews* 44(21) (2015) 7484-7539. <https://doi.org/10.1039/C5CS00303B>.
- [110] G. Bai, H.-B. Yi, H.-J. Li, J.-J. Xu, Hydration characteristics of Ca^{2+} and Mg^{2+} : a density functional theory, polarized continuum model and molecular dynamics investigation, *Molecular Physics* 111(4) (2013) 553-568. <https://doi.org/10.1080/00268976.2012.737035>.
- [111] O. Gharbi, M.T.T. Tran, B. Tribollet, M. Turmine, V. Vivier, Revisiting cyclic voltammetry and electrochemical impedance spectroscopy analysis for capacitance measurements, *Electrochimica Acta* 343 (2020) 136109. <https://doi.org/https://doi.org/10.1016/j.electacta.2020.136109>.
- [112] A. Doroszowski, The physical chemistry of dispersion, in: R. Lambourne, T.A. Strivens (Eds.), *Paint and Surface Coatings* (Second Edition), Woodhead Publishing 1999, pp. 198-242. <https://doi.org/https://doi.org/10.1533/9781855737006.198>.